De Los Santos Valladares, L, Vargas Luque, A, Borja-Castro, L, Valencia-Bedregal, R, Velazquez-Garcia, JJ, Barnes, EP, Bustamante-Dominguez, A, Byrne, P, Kollu, P, Rodriguez Martinez, M, Coaquira, JA and Barnes, CHW

Physical and chemical techniques for a comprehensive characterization of river sediment: A case of study, the Moquegua River, Peru

International Journal of Sediment Research 39 (2024) 478–494

Contents lists available at ScienceDirect

International Journal of Sediment Research

journal homepage: www.elsevier.com/locate/ijsrc

Original Research

Physical and chemical techniques for a comprehensive characterization of river sediment: A case of study, the Moquegua River, Peru

Luis De Los Santos Valladares [a, *], Arquimedes Vargas-Luque [b], Luis Borja-Castro [c], Renato Valencia-Bedregal [c], José de Jesús Velazquez-Garcia [a], Eustace Peregrine Barnes [a], Angel Bustamante Dominguez [c], Patrick Byrne [d], Pratap Kollu [e], Marco Rodriguez Martínez [f], Jose Antonio Coaquira [f], Crispin Henry William Barnes [a]

[a] Cavendish Laboratory, Department of Physics, University of Cambridge, J.J. Thomson Ave., Cambridge, CB3 0HE, UK
[b] Escuela Profesional de Ingeniería de Minas, Universidad Nacional de Moquegua, Prolongación Ave. Ancash, Moquegua, Mariscal Nieto, 18000, Peru
[c] Laboratorio de Cerámicos y Nanomateriales, Facultad de Ciencias Físicas, Universidad Nacional Mayor de San Marcos, Lima, 15081, Peru
[d] School of Biological and Environmental Science, Liverpool John Moores University, Liverpool, L3 3AF, UK
[e] Centre for Advances Studies in Electronics Science and Technology (CASEST), School of Physics, University of Hyderabad, Prof. C.R. Rao Rd, Gachibowli, Hyderabad, 500046, India
[f] Laboratory of Magnetic Characterization, Instituto de Física, Universidade de Brasília, Brasília, DF, 70910-900, Brazil

ARTICLE INFO

Article history:
Received 26 June 2023
Received in revised form
14 January 2024
Accepted 6 March 2024
Available online 8 March 2024

Keywords:
River sediment
X-ray diffraction (XRD)
Magnetometry of minerals
Mössbauer spectroscopy
Fourier transform infrared (FTIR)
Thermal analysis

ABSTRACT

River sediment is comprised of complex mineral systems composed by different kinds of organic and inorganic matter, and thus, is difficult to characterize. Besides, some standard techniques, such as X-ray diffraction (XRD), energy dispersive X-ray (EDX), optical and scanning electron microscopy, Fourier transmission infrared spectroscopy, inductively couple plasma-mass spectrometry (ICP-MS), and simultaneous Thermogravimetric Analysis – Differential Thermal Analysis (TGA-DTA), Mössbauer spectroscopy and magnetometry can provide substancial information about the compositional, physical, and chemical characteristics. In the current study, the versality of these methods is tested and the information provided by these methods for eight sediment samples, collected from the Moquegua River, Peru is compared. Qualitative analysis indicates that the samples consist of sand grains with different shapes, sizes, and colors coexisting with the presence of some diatoms. The chemical and mineralogical analysis reveal that the samples are composed mainly of silicon (Si), aluminium (Al), sodium (Na), potassium (K), aluminon–silicates, and carbonates, typical for river sediment. More detailed information obtained by these techniques include the discovery of adsorbed oxygen–hydrogen (O–H), carbon–H (C–H) and C, from organic matter, the thermal reactions and decomposition of the components, and the identification of the minor iron–oxides components. Further, other properties such as magnetic interaction are also analyzed in detail.

1. Introduction

River sediment is comprised of complex systems since they are composed of accumulated or dispersed eroded particles, organic matter, nutrients, and anthropogenic particles which are transported long distances along a basin by water. Thus, the physical and chemical characteristics of river sediment are difficult to understand and depend on surrounding conditions such as climate, geology, and anthropogenic activities (Mackenzie, 2004). Since river sediment has a large impact on the ecology, flora, and fauna, it might also affect the uses of the river water. Proper characterization of sediment composition and the determination of its physical and chemical properties are crucial for understanding the geochemical dynamics of sediment loading in almost all basins.

* Corresponding author.
E-mail address: ld301@cam.ac.uk (L.D.L.S. Valladares).

https://doi.org/10.1016/j.ijsrc.2024.03.003

In a recent study, the authors have reported the physical and chemical characterization of river sediment from the Moquegua River, Peru, by using some standard techniques such as scanning electron microscopy and X-ray dispersion spectrometry (SEM-EDX), X-ray diffraction (XRD), inductively couple plasma-mass spectrometry (ICP-MS), thermogravimetric analysis (TGA), differential thermal analysis (DTA), and Fourier transform infrared (FTIR) spectroscopy, wherein the chemical and mineralogical composition was mapped along the river and the possible anthropogenic contaminants produced by agricultural and mining activities which take place alongside the river were linked to the spatial distribution of sediment (Corzo et al., 2022; De Los Santos Valladares et al., 2022). In the previous study, a detailed explanation on how to acquire, process, and analyze the data obtained from each technique was limited. The innovation of the current study is to test and to check how the information provided by these techniques complement each other and to provide a comprehensive procedure for the characterization of river sediment rather than assessing the geochemistry of the area. Moreover, in the current study, two additional techniques, which have not been described in the

Fig. 1. Map of the Moquegua Region, Peru (taken from Google Maps, Alphabet Inc.). The sediment samples were collected from the river in Moquegua city (marked as (1) in the figure, coordinates S 17.184463°, W 70.930463°) and Ilo city (marked as (2) in the figure, coordinates S 17.622146°, W 71.342019°).

previous studies, the Mössbauer Spectrometry (MS) and Magnetometry are included, and both are useful to identify magnetic components, such as iron contained in the sediment.

2. Experimental procedures

2.1. Sites of sample collection

The Moquegua Region is located in the Andes Mountains, in South of Peru. The geology of the region is rich in copper porphyry deposits, mainly enargite (Cu_3AsS_4), encrusted in sulphide rocks such as pyrite (FeS_2, iron (II) disulphide), chalcopyrite ($CuFeS_2$), chalcocite (Cu_2S), molybdenite (MoS_2, molybdenum disulphide), galena (PbS, lead (II) sulphide), and tetrahedrite ($[Cu,Fe]_{12}Sb_4S_{13}$) (Corzo et al., 2022; De Los Santos Valladares et al., 2022). The Moquegua River has its origins in the "Cordillera Occidental" which are high Andean glaciers at elevation above the 5,000 m.a.s.l. The river crosses Moquegua City and it flows to the hyper-arid Pacific Coast at Ilo City in Southern Peru, in the course of which landscape-scale copper mining and agricultural irrigation project are being developed (Corzo et al., 2022; De Los Santos Valladares et al., 2022; Hunter et al., 2024). Eight bulk sediment samples were collected from the Moquegua River, on two different points located in Moquegua city (coordinates S 17.184463°, W 70.930463°) and Ilo city (coordinates S 17.622146°, W 71.342019°, see Fig. 1) on November 29, 2016. The depth of the river was around 0.1 m in Moquegua and from 0.1 to 1.5 m in Ilo. Figure 1 shows some photos of the places for the collection of the sediment samples. Note that while water continuously flows crossing Moquegua city, it forms a pond close to the sea in Ilo city. Furthermore, during the day of sample collection, herons were present in the Ilo site and heron guano covered many places of the study site. The samples were labeled as indicated in Table 1.

2.2. Sample processing and measurements

The sediment samples were dry in an oven overnight at 30 °C to avoid possible thermal oxidation, decomposition of organic materials, and phase transition. Thus, the analysis of the bulk sediment will only present the average of the sites of sampling. The powder X-ray diffraction studies (XRD) were accomplished using an X-ray diffractometer (XPERT PRO PANalytical, the Netherland) for the phase identification between the 2θ region of 10°–80°, where θ is the Bragg angle, the angle between the primary X-ray beam (with λ wavelength) and the family of lattice planes. The current study was done using copper (Cu)–Kα radiation with a secondary monochromator at 40 kV and 30 mA. A Jasco FTIR model 4100 spectrophotometer equipped with and Attenuated Total Reflectance (ATR) accessory was used in the FTIR spectroscopic investigations. The wave number range of this analysis was 400–4,000 cm^{-1} with the pre-set resolution of 2 cm^{-1}. The optical analysis was done using an OLYMPUS microscope model CX23 with 4 objectives of 4 ×, 20 ×, 40 ×, and 100 ×. The Scanning electron microscopy (SEM) analysis was done using a Hitachi microscope, model S–3400 N with resolution of 10 nm at 30 kV, Voltage range: 0.5 V–30 kV and magnification of 300,000 × adapted with an EDX-OXFORD Xplorer. The ICP-MS analysis (Agilent 7900) was done following a reverse aqua regia digestion in a CEM Mars 6 microwave digestion system. The relative standard deviation (RSD%) was less than 5% for all analytes. A certified reference material (CRM-016) was used to assess the accuracy and recovery of analytes in the sediment samples which was satisfactory (78%–130%) for most analytes apart from aluminium (Al) (464%), potassium (K) (276%), calcium (Ca) (9%), vanadium (V) (186%), and chromium (Cr) (183%), which were unsatisfactory.

The thermogravimetric analysis (TGA) and differential thermal analysis (DTA) were done in a LINSEIS STA PT-1600 equipment using alumina (Al_2O_3) crucibles in the range from room temperature (RT) to 1,000 °C with heating ratios of 5, 10, and 20 °C·min^{-1}. Mössbauer spectroscopy (MS) measurements were done at RT using the transmission mode geometry in a constant acceleration spectrometer with a triangular waveform and using a cobalt–57/rhodium (^{57}Co/Rh) source. Isomer shifts are quoted relative to the value of α-iron (α-Fe) thin film. The magnetic measurements were done in a DC-MPMS-SQUID magnetometer (Quantum Design Inc.) in zero field cooling (ZFC) and field cooling (FC) modes. The magnetization response as a function of the temperature was collected from 5 to 400 K and applying an external magnetic field of 1 kOe. The magnetization responses as a function of an external applied magnetic field were also measured in the range of ±5 kOe and at 5 and 300 K. Table 1 lists the amount of sample used for the TGA-DTA analysis.

3. Results and discussion

3.1. Microscopy analysis

The microscopy technique is an important and reliable method to analyze river sediment since it provides information about morphology, color, surface roughness, and particle size. The shape influences several aspects of sands and river sediments and can be of multiple forms, such as circular, spherical, cubical, elliptical, elongated, prismoid, flat, tubular, needle shaped, angular, sub-angular, surrounded, and rounded. The shape of the sediment depends, to a certain degree, on the softness of the particle materials and on degradation (Altuhafi et al., 2013; Das, 2007). Thus, circular and spherical particles provide information about the distance of travel (Dodds, 2003).

Figure 2 shows the microscopic images of the sediment samples and their size distributions. The sediment samples consist of sand particles with different colors, sizes, and shapes. The shiny surfaces infer that the samples are composed mainly of quartz, as was

Table 1
Labeling and sites of collection of samples from the Moquegua River, Peru. The mass of samples used for the Thermogravimetric Analysis – Differential Thermal Analysis (TG-DTA) measurements at different temperature rates and grain sizes estimated from the optical microscopy analysis also are listed. The ± (plus or minus) sing indicates the error in each figure.

Site	Sample Label	Shore	Shore	Mass for TGA-DTA (mg)			Mean Size (μm)
				5 °C·min^{-1}	10 °C·min^{-1}	20 °C·min^{-1}	
Moquegua	M1	Out of the river	Surface	22.2	21.2	22.2	139 ± 0.8
	M2	Out of the river	5 cm	22.4	22.9	22.2	251 ± 15.7
	M3	Into the river	Surface	22.6	22.5	22.4	525.8 ± 26.7
	M4	Into the river	10 cm	21.6	21.8	21.6	333.5 ± 44.0
Ilo	I1	Out of the river	Surface	23.8	23.6	23.1	572.9 ±
	I2	Out of the river	5 cm	23.5	23.3	23.4	458.6 ± 9.6
	I3	Into the river	Surface	23.7	23.4	23.7	478.7 ± 8.9
	I4	Into the river	10 cm	23.3	23.4	23.4	758.1 ± 13.8

confirmed by the X-ray analysis described later. However, samples M1, I1, I2, and I3, unlike the others, contain some dust suggesting that they are composed by two kinds of sand with different formation stories. In addition, diatoms were observed on sample I3 (see Fig. S1 in the Electronic Supplementary Material (ESM) S1), as expected since the sample was collected from the surface bed of the river, close to the sea, where diatoms are the main components of phytoplankton (de Vries & Schrader, 1981; Hutchins et al., 2002).

The histograms shown in Fig. 2 correspond to each micrograph. The mean diameter sizes for all the samples are listed in Table 1. It has been reported that sands with fine grains are capable for retaining more water than those with large diameter (Haghighizade et al., 2017). According to Table 1, the sample with the smallest mean size is M1 (about 139 ± 0.8 μm), whereas the sample with the largest mean size is I4 (758.1 ± 13.8 μm) and the sizes of the other samples are between these values.

The shape of the grains also gives information with respect to if the sediment has interacted with calm or dynamic water. Note that for samples M1, M4, I1, I2, and I4, their shape is prismoid, whereas the shape of the grains of samples M3 and I3 are elongated and low rounded. Rounded grains, as in samples M2 and M4, indicate that the particles have been in continuous crashing with others (Alshibli & Alsaleh, 2004; Lorenz & Zimbelman, 2014).

Figure 2 also shows the SEM micrographs for all the samples. The SEM micrograph for each surface consists of microcomponents of different shapes and sizes. The use of a SEM allows the information about the micro-morphology of the surface and subcomponents of individual grains (Smart & Tovey, 1981). It was not possible to estimate the mean size of these components since they are stuck and accumulated. Different magnification micrographs are given in the ESM S1.

3.2. Chemical and mineralogical analysis

The X-ray techniques are crucial to study the chemical and mineralogical composition of river sediment. The two most useful X-ray techniques are EDX and XRD. EDX provides information on the major chemical components on the sediment samples. For example, it can effectively detect the calcium oxide/silicon dioxide (CaO/SiO_2) ratio in sands. XRD is useful not only for identifying the mineralogical composition, but also for testing the crystallinity of quartz, silicates, and other mineral components in the sand and sediment. For example, it has been

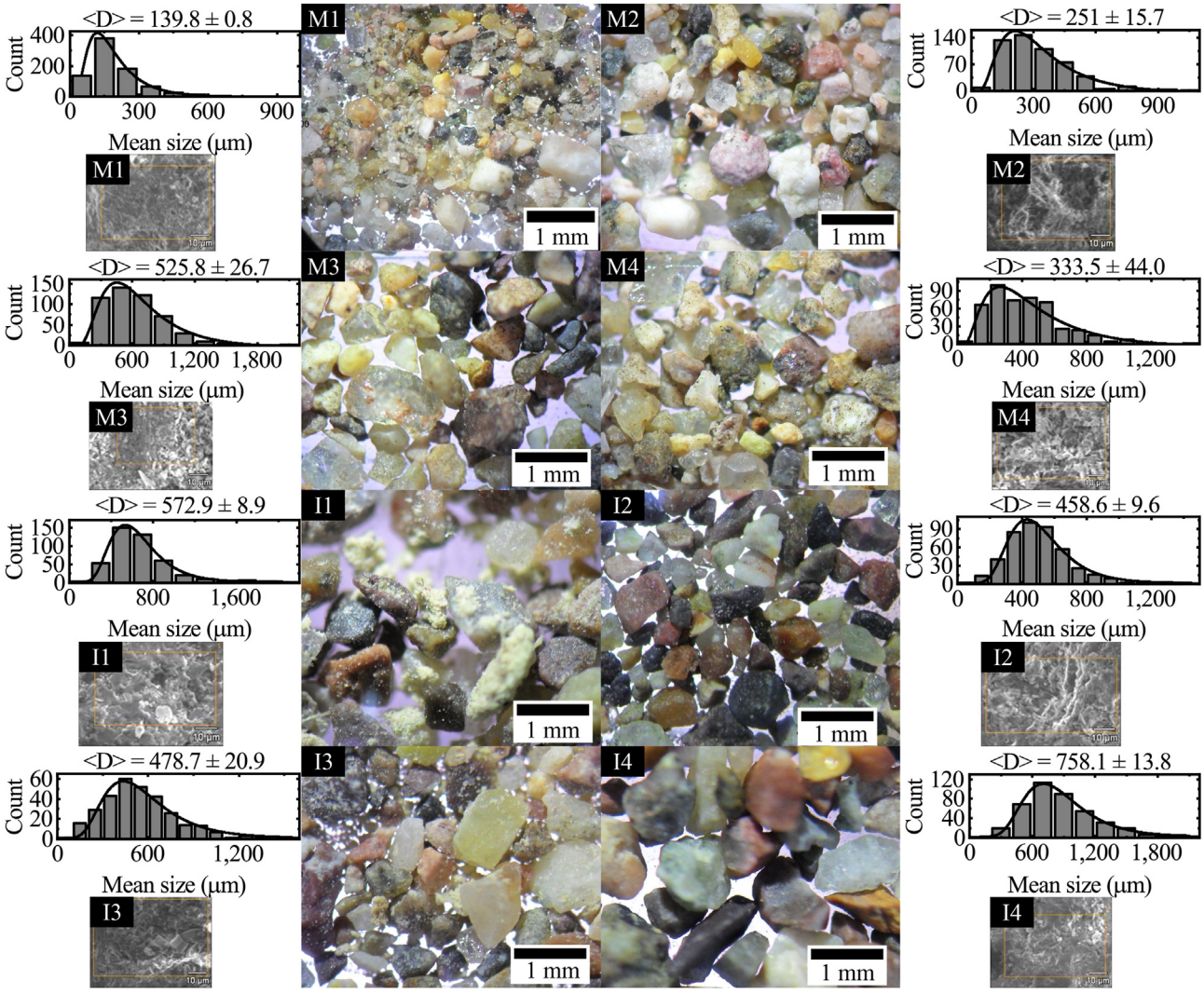

Fig. 2. Microscopy analysis and histograms of sediment samples collected from two different sites from the River Moquegua, Peru (I: Ilo, M: Moquegua). The ± (plus or minus) sing indicates the error in each figure.

reported that the crystal index of quartz decreases with depth of collection (Ramasamy et al., 2004). Moreover, XRD also gives information of the crystallite sizes by estimating the peak intensity of the diffraction pattern (Thamaphat et al., 2008).

The ESM S2 shows the EDX spectra for the samples. The chemical composition was determined over the rectangular areas marked in each SEM images, shown in Fig. S1 in the ESM S1. The quantification of the chemical elements is listed in Table 2. According to Table 2, all the samples contain silicon (Si), aluminum (Al), calcium (Ca), sodium (Na), and oxygen (O) as the most abundant elements. This was expected since the main composition of river sands and rocks are quartz (SiO_2) and alumina–silicates ($xAl_2O_3 \cdot ySiO_2 \cdot zH_2O$, where x, y, and z can be Na, Ca, and potassium (K), respectively) minerals (Frondel, 1962; Gudbrandsson, 2013). In fact, according to the XRD analysis (see Fig. 3 and Table 2), the mineralogical composition for almost all the samples contains quartz, and Na– and Ca–Al silicates.

ICP-MS is a laboratory-based analytical approach for determining element concentrations in aqueous media, or in solid samples that have undergone a digestion and extraction procedure. The ICP (Inductively Coupled Plasma) is a high temperature ion source, which ionizes the sample. The MS (Mass Spectrometer) is a charge/mass analyzer which separates all elements simultaneously; the ions are measured simultaneously with the mass detector at the ppm (part per million) level. During the analysis, the elements in the sample are ionized in the ICP part and sent to the MS section. The approach gives greater accuracy and limits of detection than the other elemental analysis approaches (e.g., SEM-EDX) used herein. The major element concentrations from the ICP-MS analysis also are listed in Table 2.

The main type of silicate component found in samples M1, M2, M3, I2, and I3 was albite ($AlNaSi_3O_8$). Albite is a plagioclase tectosilicate usually occurring in white color which indicates that those grains showing whiter color in the optical images (Fig. 2) might contain more albite. Albite crystallizes with triclinic pinacoidal shape and it occurs in two variants referred as low albite and high albite (Tuttle & Bowen, 1950). Although both variants are triclinic, they differ in the volume of their unit cell, which is slightly larger for the high form. The high form can be produced from the low form by heating at around 700–800 °C.

Extensive agricultural areas lie next to the Moquegua River. Local farming uses a variety of fertilizers such as potassium chloride

Table 2
Chemical abundance obtained using EDX and ICP-MS, and Mineralogical composition obtained by XRD analysis of river sediment collected from Moquegua and Ilo cities, Peru.

Moquegua city sample				
Technique	M1	M2	M3	M4
EDX (wt%)	O (49.78) Si (31.60) Al (8.19) C (3.95) K (2.98) Fe (1.94) Mg (0.78) Ca (0.79)	O (41.65) Si (18.25) Fe (14.18) C (11.49) Al (6.81) Ca (2.74) Mg (2.30) Na (1.34) K (0.60)	O (39.95) Si (31.91) Al (8.97) C (6.92) Na (6.64) Mn (4.25) Ca (1.36)	O (44.05) Si (28.35) C (9.17) Al (8.55) Fe (3.70) Na (3.58) K (1.60) Ca (1.01)
ICP-MS (%)	Si (19.1) Al (7.32) Mn (2.11) Na (1.99) K (1.78) Fe (1.32) Ca (0.56) Mg (0.55)	Si (15.4) Fe (12.32) Al (5.43) Mg (1.89) Ca (1.78) Mn (1.67) Na (1.07) K (0.33)	Si (27.7) Fe (7.89) Al (5.67) Mn (3.11) Na (1.72) Ca (1.34) K (0.56) Mg (0.54)	Si (22.9) Al (7.76) Mn (3.12) Fe (2.34) Na (1.87) K (1.34) Ca (0.89) Mg (0.81)
XRD	Quartz (SiO_2) Albite ($NaAlSi_3O_8$)	Quartz (SiO_2) Cristobalite (SiO_2) Hematite (α-Fe_2O_3)	Quartz (SiO_2) Cristobalite (SiO_2) Albite ($NaAlSi_3O_8$) Magnetite (Fe_3O_4)	Quartz (SiO_2) Calcite ($CaCO_3$) Sillimanite (Al_2Si_5)
Ilo city sample				
Technique	I1	I2	I3	I4
EDX (wt%)	O (46.39) Si (32.25) C (9.09) Al (4.94) K (4.77) Ca (1.37) Na (1.19)	O (41.42) Si (31.08) Al (7.60) K (5.22) C (5.07) Fe (4.18) Na (2.54) Ca (1.53) Mg (1.34)	O (47.12) Si (31.99) C (6.99) Al (6.26) Na (2.65) Ca (2.08) S (0.46)	O (45.78) Si (28.61) C (10.22) Al (7.24) Na (3.40) K (3.28) Fe (1.47)
ICP-MS (%)	Si (29.1) K (4.23) Fe (4.21) Al (4.11) Ca (1.01) Na (1.01) Mn (0.76) Mg (0.21)	Si (27.8) Al (5.43) K (4.23) Fe (3.99) Na (2.11) Ca (1.34) Mg (0.76) Mn (0.56)	Si (23.5) Al (5.39) K (3.81) Fe (2.91) Na (2.01) Mn (1.87) Ca (1.65) Mg (0.19)	Si (23.3) Al (6.99) K (2.45) Na (1.89) Mn (1.52) Fe (1.09) Ca (1.01) Mg (0.54)
XRD	Quartz (SiO_2) Dolomite ($MgCaCO_3$) Low Albite ($NaAlSi_3O_5$)	Quartz (SiO_2) Magnesium Silicate (MgSiO) Albite ($NaAlSi_3O_5$)	Quartz (SiO_2) Dolomite ($MgCaCO_3$) Low Albite ($AlSi_3O_5$)	Quartz (SiO_2) Cristobalite (SiO_2)

Note: Mn – manganese; C – carbon.

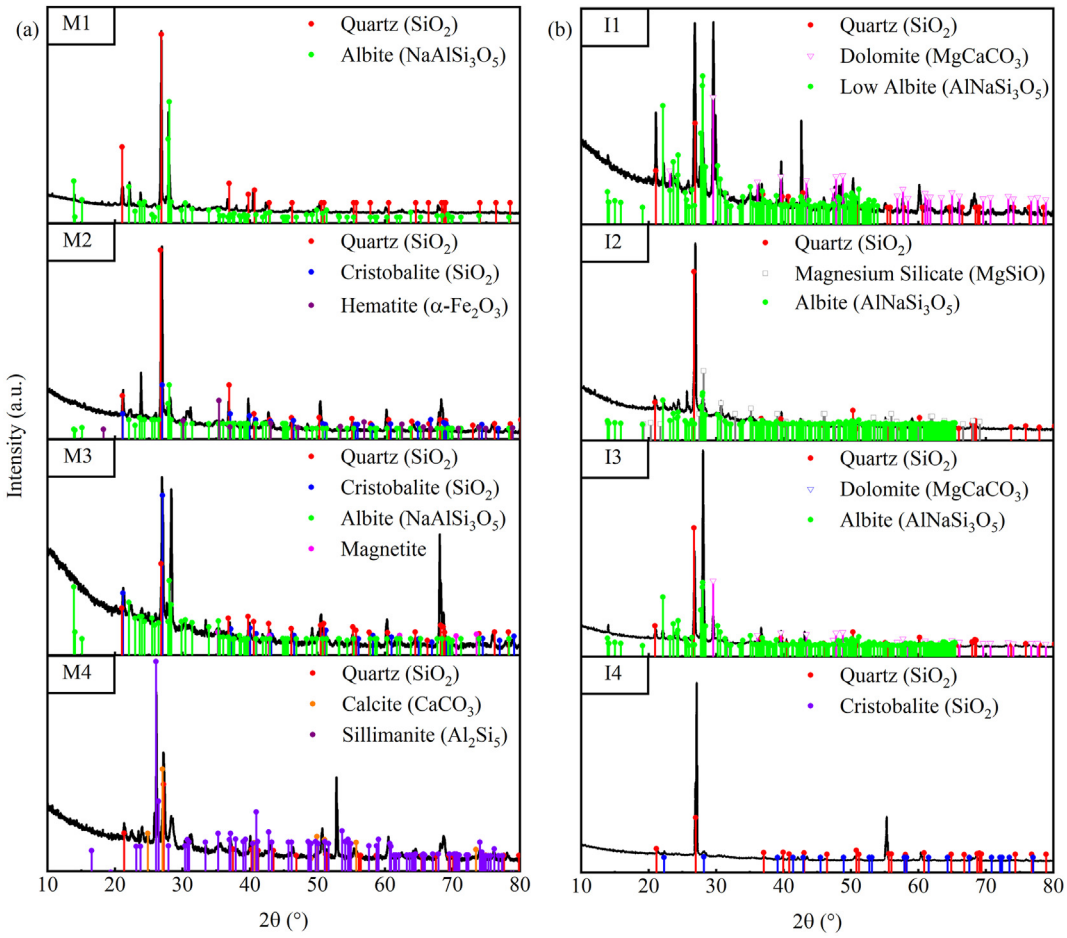

Fig. 3. Mineralogical composition of the sediment collected from two points along the Moquegua River. (a) Sediment collected in Moquegua city and (b) sediment collected in Ilo city.

(KCl, containing 60 wt% (K_2O)), potassium sulphate (K_2SO_2, containing 50 wt% K_2O and 18 wt% (S)), magnesium sulphate heptahydratated ($MgSO_4 \cdot 7H_2O$, containing 16 wt% (MgO) and 13 wt% phosphorus pentoxide (P_2O_5) and 15 wt% Ca) and a fertilizer called "compound 20-20-20" (containing 20 wt% nitrogen (N), 20 wt% P_2O_5 and 20 wt% K_2O) (Corzo et al., 2022; De Los Santos Valladares et al., 2022). The EDX analysis detects K in all the samples, which together with nitrogen and phosphorous, are essential macronutrients for plant nutrition and are used as one of the main components of fertilisers in agriculture (Ajasa et al., 2004; Liu et al., 2009), especially in the form of potassium chloride (KCl, Sylvite) (Meena et al., 2016; Webb, 1939). Note that XRD does not detect any mineral composed of K, this might be due to its low concentration as EDX has shown. Therefore, it is not clear if potassium comes from natural minerals or from the rest of the fertilizers used by the local farmers. Similarly, some traces of magnesium (Mg) have been also detected using the EDX technique in samples M1, M2, and I3. Magnesium is a secondary macronutrient (Ajasa et al., 2004; Liu et al., 2009). The outstanding role of magnesium in plant nutrition is as a constituent of the chlorophyll molecule. As a carrier, magnesium also is involved in numerous enzyme reactions as an effective activator, in which it is strongly associated with energy-supplying phosphorous compounds (Härdter et al., 2005; Uebel & Heinsdorf, 1997). Magnesium is very mobile in plants, and, like potassium, when deficient is translocated from older to younger tissues (Härdter et al., 2005), so that signs of deficiency appear first on the oldest tissues and then spread progressively to younger tissues. The magnesium might come from nor natural MgO (periclase) not detected by XRD or from magnesium calcite ($MgCaCO_3$) found in samples I1 and I3.

The energy dispersive X-ray technique also detects calcium in almost all the samples which should come from calcium carbonate limestones formed from bones, shells, and scallops. Indeed, the XRD technique reveals the presence of $MgCaCO_3$ as the main component of samples I1 and I3 and, calcium carbonate ($CaCO_3$) for sample M4. Thus, the Ca found in almost all the samples should come from limestone.

Iron also is detected by the EDX technique in most of the samples, with relatively high concentration in sample M2 (14.18 wt%). Since metallic iron is rarely found in nature because it tends to oxidize, the Fe detected by EDX might come from any iron minerals such as hematite (α-Fe_2O_3) (De Los Santos Valladares et al., 2019; Leon et al., 2011) or magnetite (Fe_3O_4), those minerals were detected for samples M2 and M3, respectively by XRD. Note that XRD does not detect any further Fe minerals in the rest of the samples possibly due to their low amount. Since most of the iron oxides are hard ferro- or ferri-magnetic, they also might be detected by measuring their magnetic properties.

3.3. FTIR analysis

Minerals have few but more intense infrared (IR) absorption bands than most organic compounds. This is reflected in sediment because they consist of composites of many minerals together with

a certain amount of organic matter (Ramasamy et al., 2009). In sediment, the assignation and identification of inorganic compounds is more complex than for the organic counterparts due to the wide and irregular absorption bands (Reig et al., 2002). The structure of the compound plays a crucial role in the appearance of the spectra, as compounds with the same chemical composition but different structure will show different spectral profiles (Reig et al., 2002). The FTIR spectra of all the samples from both rivers are shown in Fig. 4. The proposed composition and corresponding wave numbers per sample is listed in Table 3. The results demonstrate that most of the samples are composed of quartz, feldspars, clay minerals, absorbed water, and organic matter. Other components in lower quantity have also been proposed such as Hematite and inorganic carbonates.

The similitude of all the FTIR spectra facilitates the identification of components by dividing the samples in different regions. The region of 3,000–3,800 cm^{-1} mainly corresponds to hydroxide (OH) stretching as well as the 1,600–1,700 cm^{-1} due to the OH bending modes of water and hydroxyls (Allard et al., 2002; Parikh et al., 2014; Ramasamy et al., 2009).

The bands at the region between 2,000 and 3,000 cm^{-1} indicates the presence of organic matter, although some bands overlap other regions. The bands in the region of 1,200–2,000 cm^{-1} mainly show the overtones of quartz although calcite and organic matter also are identified in this region (Allard et al., 2002). The region of 900–1,200 cm^{-1} exhibit the Si(Al)–O stretching vibration while Si–O symmetrical stretching and other bending vibrations occurs at lower wave numbers. The results presented here, with few exceptions, agree with the absorption maxima reported in the literature.

In the current study, the FTIR results agree with the XRD results that silicates are the main constituent of the sediment on both sites on the river. Quartz seems to be the most abundant and common mineral component in most of the samples at both sites. The presence of quartz is demonstrated by the Si–O asymmetrical vibrations around 1,090 and 1,158 cm^{-1} (Anbalagan et al., 2010; Ilia et al., 2009; Ramasamy et al., 2009; Roy, 1987). The shift of the pure silicate band at 1,100 cm^{-1} to a lower wave number due to the presence of aluminium or iron in the lattice and then the presence of other silicate minerals such feldspars and clays (Anbalagan et al., 2010; Roy, 1987). The doublet around 795 and 780 cm^{-1} suggest the silica is in form of α-quartz (Anbalagan et al., 2010). Eventually, seven peaks at 1,995, 1,870, 1,684, 1,610, 1,525, and 1,492 cm^{-1} are overtones and combinations of the Si–O vibrations of quartz (Igisu et al., 2006; Ito & Nakashima, 2002). Therefore, quartz is present in all samples and mainly as α-quartz phase.

In contrast to XRD results, amorphous silica is difficult to determine by FTIR when crystalline quartz and other silicate minerals are present. However, the presence of amorphous silica could partially explain the shift of maximum absorption around 1,100 and 3,300 cm^{-1} (Meyer-Jacob et al., 2014; Ojima, 2003). Therefore, it is proposed here that amorphous silica is main component in samples M1, M2, M3, I3, and I4.

Clay minerals are common components of sediment from rivers and their absorption bands can overlap with those of quartz, amorphous silica, and feldspars. Nevertheless, the absorption bands around 3,690 and 3,620 cm^{-1} usually are associated with the internal surface OH groups in kaolinite (Khang et al., 2016; Madejová, 2003; Ramasamy et al., 2009; Tao et al., 2014; Temuujin et al., 2001; Tironi et al., 2012). The absence of the band at 3,670 and 3,653 cm^{-1} indicates a disordered phase of kaolinite (Tironi et al., 2012). Additionally, the amorphization of the kaolinite merges the three peaks due to the Si–O stretching usually seen at 1,105, 1,032, and 1,010 cm^{-1} into one broad band around 1,029 cm^{-1} (Ramasamy et al., 2009; Tao et al., 2014; Temuujin et al., 2001). The aluminium hydroxide (Al_2OH) bending bands from vibrations of inner and surface OH groups arise at 914 cm^{-1} (Madejová, 2003; Vaculíková & Plevová, 2005). Most of those are present in samples M1–M4 but absent in samples I1–I4, which suggests a slight change in chemical composition between the Moquegua and Ilo sediment.

The absence of the 3,690 cm^{-1} and the presence of 3,653 cm^{-1} in the samples from Ilo may indicate the presence of different clay minerals. Therefore, the bands around 3,653, 1,020, and 848 cm^{-1} are, respectively, assigned to stretching OH groups laying between the tetrahedral and octahedral sheets, Si–O stretching, and OH deformation bands in montmorillonite (Ramasamy et al., 2009; Vaculíková & Plevová, 2005). The broad OH–stretching band around 3,653 cm^{-1} may correspond to the wide envelope of Al–Al–OH and Al–Mg–OH environments in highly substituted and distorted montmorillonites (Vaculíková & Plevová, 2005). Therefore, kaolinite is proposed to be present in all the samples from Moquegua and montmorillonite in all the samples from Ilo.

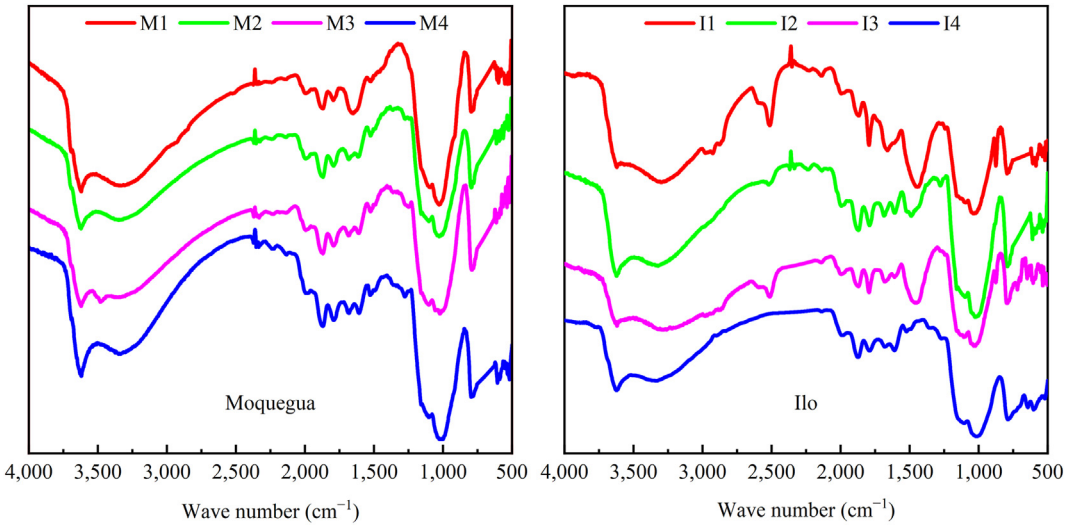

Fig. 4. FTIR spectra of the sediment samples collected from two points along the Moquegua River. (a) Sediment collected at Moquegua. (b) Sediment collected at Ilo.

Table 3
Observed frequencies of in 1 cm^{-1} with corresponding component in the sample and the tentative assignment.

Component	M1	M2	M3	M4	I1	I2	I3	I4	Tentative assignment
Quartz	1,994	1,994	1,993	1,994	1,994	1,994	1,993	1,987	Overtone
	1,869	1,869	1,869	1,870	1,869	1,870	1,869	1,873	Overtone
	1,793	1,792	1,793	1,793	1,794	1,791	1,793	1,789	Overtone
		1,682	1,685	1,680	1,660	1,686	1,680	1,681	Overtone
		1,615	1,609	1,607		1,608	1,609	1,609	Overtone
	1,522	1,524	1,525	1,526		1,515		1,521	Overtone
				1488		1,488		1492	Overtone
	1,159	1,157	1,157	1,158	1,158	1,158	1,158		Si–O asymmetrical vibration
	1,092				1,094	1,097	1,095		Si–O asymmetrical vibrations
	796	794	790	795	794	790	797		Si–O symmetrical stretching
	780	779	780	779	780	783	778		Si–O symmetrical stretching
Amorphous silica		1,102	1,102	1,103			1,107	1,104	Si–O stretching
Kaolinite	3,693	3,692	3,690	3,691					OH stretching vibration
	3,620	3,621	3,621	3,619					OH stretching vibration
	1,028	1,027	1,022	1,024					Si–O stretching
	914								Al_2OH bending bands
Montmorillonite					3,621	3,622	3,619	3,622	OH stretching vibration
					1,022	1,023	1,024	1,020	Si–O stretching
					848	848	848		OH bending
Albite		1,102	1,102	1,103			1,107	1,104	Si–O stretching
								787	Si–Si(Al) stretching
							640	643	O–Si(Al)– bending
	608	604		605	607		605	602	O–Si(Al)– bending
		428	429		425	426		427	O–Si–O deformation
Organic matter								3,482	OH alcohols and carboxylic acids
					2,979		2,981		C–H stretching CH_3
	2,928				2,926			2,901	C–H stretching CH_2
	2,854				2,877		2,881		C–H stretching CH_2
			1,249	1,275	1,273	1,277		1,270	OH deformation phenolic groups
Water	3,333	3,348	3,339	3,336	3,296	3,321	3,293	3,336	OH stretching of adsorbed water
	1,649								OH bending of adsorbed water
Dolomite						2,588		2,592	C–O symmetric stretching
Calcite						2,512	2,524	2,512	OH stretching
					1,444	1,462	1,459		$(CO_3)^{-2}$ stretching
Hematite	532		536	532	535	536	535	535	Fe–O

Although the XRD analysis of the samples identify the presence of albite in almost all the samples, the main bands of this phase overlaps with quartz and clay minerals bands which makes the identification difficult. However, it is suggested that the small shift in the band at 1,092–1,102 cm^{-1} for samples M2, M3, M4, I3, and I4 may be due to the presence of both amorphous silica and albite. Additionally, the bands around 643, 602, and 427 cm^{-1} are identified as Si–O stretching, O–Si(Al)–O bending, and O–Si–O deformation, respectively (Senthil Kumar & Rajkumar, 2013; Theodosoglou et al., 2010; Zhang et al., 1996). Therefore, it is considered that albite is one of the mayor components of all samples as it is suggested by the XRD analysis.

The bands around 2,928 and 2,854 cm^{-1} correspond to C–H stretching vibrations of methylene (CH_2) groups while the band around 2,980 cm^{-1} is assigned to C–H stretching vibrations of methyl (CH_3) groups (Igisu et al., 2006). The band between 1,240 and 1,280 cm^{-1} is assigned to the O–H stretching of phenolic –OH (Fu & Quan, 2006). Eventually, the strong band around 3,482 cm^{-1} is proposed to come from O–H vibrations of organic compounds (Yoo et al., 2016).

The presence of water may have diverse sources: that coming from the organic matter and adsorbed by clay minerals and amorphous silica. The broad band at 3,333 cm^{-1} corresponds to H–O–H vibrations of adsorbed water and this band is intensified in some samples due to the increase of adsorbed water due to a more amorphized structure of the clay minerals or higher presence of organic matter (Tao et al., 2014; Temuujin et al., 2001). The additional band around 1,649 cm^{-1} corresponds to the bending vibrations of unbound adsorbed water molecules (Ramasamy et al., 2009; Yoo et al., 2016).

Carbonates also are common in river sediment and their presence is demonstrated by $(CO_3)^{-2}$ stretching at bands around 1,444 cm^{-1} at I1, 1,462 cm^{-1} at I2, and 1,459 cm^{-1} at I3 (Ramasamy et al., 2009; Senthil Kumar & Rajkumar, 2013; Vogel et al., 2008). Additionally, the band around 2,588 cm^{-1} is characteristic of dolomites while 2,512–2,524 cm^{-1} of calcites at I1, I2, and I3 are assigned to carbonates (Ji et al., 2009; Ramasamy et al., 2009; Rosén et al., 2010; Stanienda, 2016; Vogel et al., 2008). The mineral form of the iron (III) oxide (α-Fe_2O_3, hematite) is usually detected by an adsorption band at 530 cm^{-1} (Ramasamy et al., 2009; Senthil Kumar & Rajkumar, 2013). This band is found in all the samples.

3.4. Thermal analysis (TGA-DTA)

The thermogravimetric analysis technique can be used to estimate the chemical weathering, dehydration, phase transition, and water and carbon release in sediment. Trough DTA one can provide information on the transformation that has occurred in the sample during the temperature increase, such as glass transitions, crystallization, decomposition, sublimation, and melting processes (Berger & Akehurst, 1966; Hatakeyama & Liu, 1998).

Figure 5 shows the TGA-DTA measurements for all the samples taken at a heating rate of 5 °C·min^{-1}. The loops obtained at heating rates 10 and 20 °C·min^{-1} are given in the ESM S3. Unexpectedly, the TGA thermograms for most of the samples show an increase in mass between 4 and 8% starting from RT and even up to 1,000 °C. This apparent increase in mass might be caused by the "buoyancy effect" produced by the empty reference crucible generating a reinforced lifting effect in the temperature range of measurement (Newkirk, 1960), together with reactions, such as adsorption,

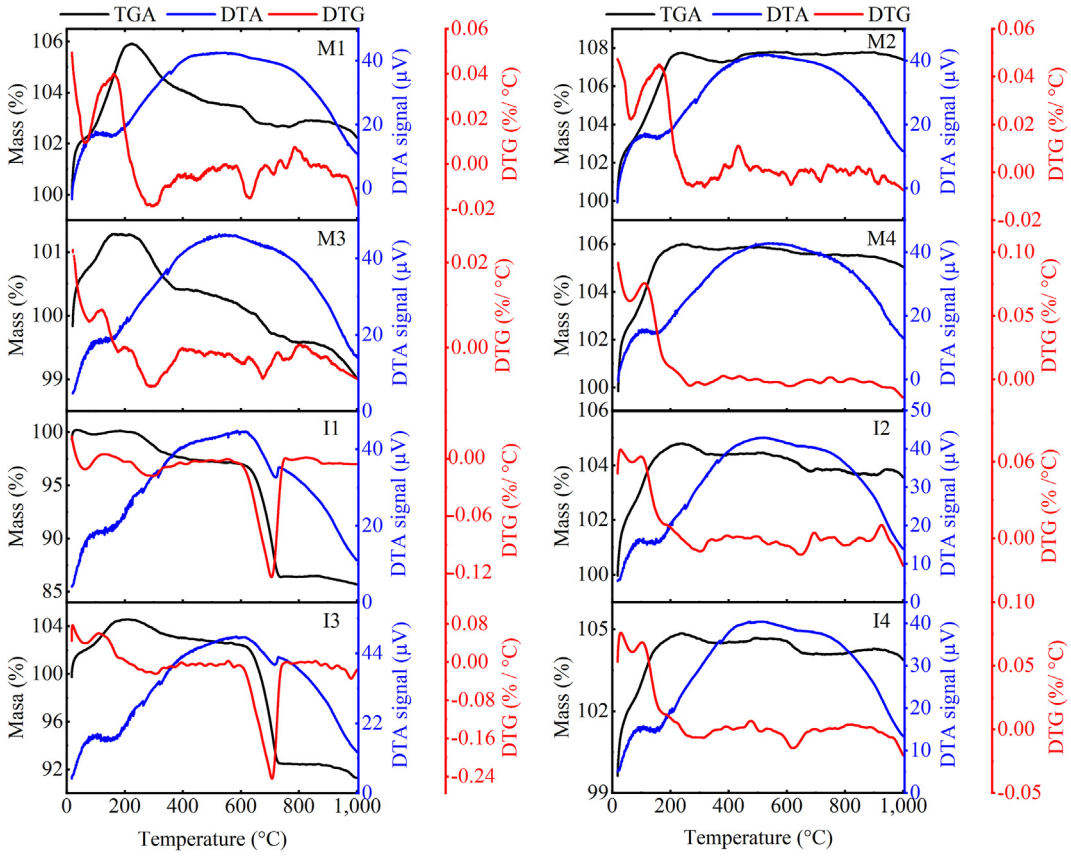

Fig. 5. TGA-DTG and DTA of the samples M1–M4 and I1–I4 from room temperature to 1,000 °C, obtained at increase rate of 5 °C·min^{-1}. There are remarkable differences among the DTA Curves in the range of 100–400 °C and 600–900 °C for samples I1 and I3, respectively. The curves obtained at 10 and 20 °C·min^{-1} rates are contained in the ESM S3.

absorption, oxidation, or solid–gas reaction, which occur during heating (Dunn, 2000; Newkirk, 1960). All the changes in mass previously mentioned are listed in Table 4. For the samples collected from 5 to 10 cm deep from the surface of the sites, the mass do not change even up to 1,000 °C suggesting that those samples retained more water than the samples collected from the surface. In the chemisorption phenomenon, organic components in minerals tend to gain mass during heating in the temperature range of 200–500 °C and this gain tends to be lost due the ignition process which continues up to 800 or 850 °C. If this does not occur, mineral samples tend to lose mass between 250 and 850 °C (Carol et al., 2012). In the current study, a decrease in mass was observed even up 1,000 °C, which might be caused by the ignition of the organic components as in the case of samples M1 and M2, or the annealing of organic material followed by the decomposition of some minerals as in the case of samples I1 and I3 (Carol et al., 2012).

Above 200 °C, the TGA loops present weight losses which should be caused by the release of water, volatile organic matter, and some minerals decomposition (Gaál et al., 2007; Schnitzer et al., 1964). However, the TGA for the samples collected from bank and bed excavations reveal only minor weight losses. This information is useful for further studies about the chemical weathering properties and erosion of soils in the area since the weight loss (W_{loss}) values provide semi-quantitative information about the wettability and hygroscopic properties of the sediment samples (Gaál et al., 2007; Schnitzer et al., 1964). Hygroscopic properties of sediment usually depend on many factors such as salt composition, porosity, granularity, organic composition, and other related processes. It has been reported that sediment containing iron quickly dehydrate with the increase of temperature to form iron oxides (Dinnis, 1994). If that is the case, water should dehydrate easier in those samples containing high concentrations of iron. This suggestion might match with the weight loss in the TGA loops for samples M1 and M3. However, as previously discussed, this element is present in most of the samples, and most of them do not follow this assumption. Therefore, the hygroscopic properties of the sediment should be also related to other physical or chemical properties of the samples (porosity, organic components, etc.).

Gaál et al. (2007) proposed that water also binds on the surface of the sediment particles by adsorption and those grains containing more organic material bind more water due to colloid chemical forces. This concept is consistent with (Oudghiri et al., 2014, 2015a, 2015b) who also proposed that Differential Thermal Gravimetry (DTG) loops of sediment show a big peak at around 200–300 °C for

Table 4
Change in mass (%) during thermogravimetry analysis of river sediment collected from Ilo and Moquegua cities. The measurements were taken at different rates of temperature increase of 5, 10, and 20 °C·min^{-1}.

Scan rate	M1	M2	M3	M4	I1	I2	I3	I4
5 °C·min^{-1}	5.95 (~250 °C)	6.63 (at ~250 °C)	1.27 (at ~250 °C)	5.96 (at ~250 °C)	−0.34 (at ~100 °C)	4.80 (at ~250 °C)	4.54 (at ~250 °C)	4.83 (at ~200 °C)
10 °C·min^{-1}	−1.58 (at ~200 °C)	1.71 (at ~60 °C)	1.05 (at ~150 °C)	1.05 (at ~100 °C)	2.36 (at ~110 °C)	4.7 (at ~250 °C)	5.8 (at ~200 °C)	6.64 (at ~600 °C)
20 °C·min^{-1}	−0.86 (at ~110 °C)	0.98 (at ~100 °C)	1.39 (at ~150 °C)	1.06 (at ~300 °C)	0.087 (at ~100 °C)	−1.16 (at ~150 °C)	−0.097 (at ~110 °C)	3.66 (at ~600 °C)

high concentrations of organic components and a peak at around 600–700 °C for high concentrations of inorganic carbon. Note that the DTG loops for most of the samples have big peaks around 300 °C following the assumption that the amounts of organic components in the samples are insufficient to retain water molecules when increasing the temperature; therefore, no loss mass is detected due dehydration for temperatures less than 300 °C for almost all the sediment samples. According to Fig. 5, the highest weight losses are observed for samples I1 and I3 in the range of temperature of 600–700 °C, which are 11% and 10%, respectively, due the decomposition of magnesium calcium carbonate ($MgCaCO_3$) (Dweck et al., 2000). This is accompanied with the big peak around 700 °C in the DTG loops and the endothermic peak on the DTA curves, which starts at 619 up to 730 °C for both samples. These results also are consistent with the assumption of Oudghiri et al. (2014, 2015a, 2015b) that the loss of mass at 600–700 °C is caused by the presence of inorganic C in the dolomite mineral ($MgCaCO_3$) detected by the XRD analysis as can be seen in Fig. 4. On the other hand, the decomposition of calcium carbonate occurs by volatilization, i.e., $CaCO_3 \rightarrow CaO + CO_2$ (carbon dioxide); however, although $CaCO_3$ was detected by XRD in sample M4, its decomposition with increases in the temperature was not detected in the thermograms meaning that this sample is not homogeneous. This was also suggested by the FTIR analysis which does not show any vibrational mode for this sample.

In addition, the release of CO_2 increases with temperature. This carbon dioxide should react with the hot surrounding air to form a weak acid creating a broad exothermal peak in the DTA loops between 350 and 650 °C (Carol et al., 2012; Oudghiri et al., 2014, 2015a, 2015b). This process of burning organic matter makes the samples lose some mass, as confirmed by the TGA loops. On the other hand, mineral phase transitions are better detected by the formation of sharp exothermic peaks in the DTA plots occurring at temperatures higher than 1,200 °C (Tuttle & Bowen, 1950), well above the current measurement conditions.

3.5. Mössbauer analysis

For qualitative analyses of rocks, soils, and sediment, Mössbauer Spectroscopy (MS) with a ^{57}Fe source allows the identification of each one of the various iron-bearing species present in the sample. The appearance of the typical spectra, defined by their specific hyperfine parameters, enables, in many cases, immediately assignment of the unknown phases in the sample. Among the applications in sediment, the oxidation state of iron allows information about the oxidation-reduction conditions of sedimentation to be obtained (Bancroft, 1973). Using this technique, the oxidation state, spin state (low or high spin state), coordination number, magnetic properties, magnetic transition phases, site symmetry, and lattice dynamics of iron components in the sediment can also be investigated (Greenwood & Gibb, 1971). Though detailed studies have been demonstrated that Mössbauer spectroscopy is applicable in the characterization of multiple assemblages and in the determination of site populations of Fe^{2+} in silicate minerals (Bancroft, 1973; Bancroft et al., 1967; Bowen & Weed, 1984; Tominaga & Minai, 1984). Mössbauer spectroscopy also is well recognized as a powerful tool for the determination of the Fe^{3+}/Fe^{2+} ratio (Minai & Tominaga, 1982) and semiquantitative determination of the distribution of iron among different minerals and lattice sites which is possible with doublets and sextets spectra distributions.

The ability of Mössbauer spectroscopy to discriminate between Fe(III) and Fe(II) in various minerals (clay minerals, oxides, sulphides, carbonates, etc.) is of great importance to geochemists, because the geochemical reactivities of the species are not the same. One example of interest is the current geochemical modelling of Fe diagenesis that only considers the Fe oxides as reactive, whereas the Fe within the clay minerals is neglected (van Cappellen & Wang, 1996; Wang & van Cappellen, 1996). The preservation of the sample must be maintained when performing several techniques for non-interfering in different analyses. Mössbauer spectroscopy fulfils this requirement for comparison, for instance, with atomic absorption spectrometry that is used for the determination of Fe in sediment and mineral samples, providing information concerning the total concentration but atomic spectroscopy technique requires the sample to undergo destructive pre-treatment processes.

The typical experimental spectra and the fitting curves are shown in Fig. 6. All experimental Mössbauer spectra were fitted by Lorentzian profiles and the fitted Mössbauer spectra parameters are listed in Table 5. All spectra show a well-developed magnetic

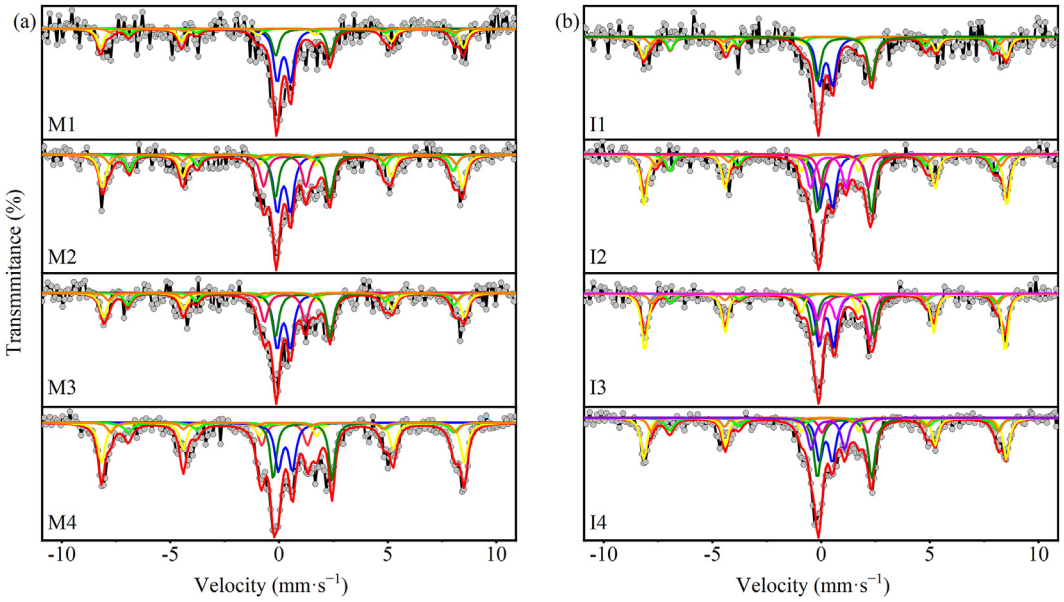

Fig. 6. Mössbauer spectra of eight sediment samples collected from the Moquegua River, Peru, at two points: (a) Moquegua city and (b) Ilo city. The dots are the experimental data obtained at room temperature, the solid red line is the resulting spectrum, and the other solid lines of distinct colors are the subspectra.

Table 5
Mössbauer spectra parameters obtained from the fit of the room temperature spectra from the sediment samples collected from the Moquegua river at Moquegua and Ilo cities, Peru.

Sample	Spectra	Fe^{3+}/Fe^{2+}	I.S. ($mm \cdot s^{-1}$)	Q.S. ($mm \cdot s^{-1}$)	B_{hf} (T)	W ($mm \cdot s^{-1}$)	A (%)
M1	FeS_2 (Pyrite)	Fe^{3+}	0.32	0.62	—	0.39	37
	$Ca_2Fe^{2+}(PO_4)_2 \cdot 4H_2O$ (anapaite)	Fe^{2+}	1.18	2.50	—	0.39	20
	Magnetite (Fe_3O_4)	$Fe^{2.5+}$	0.66	—	46.3	0.40	10
		Fe^{3+}	0.28	—	49.2	0.38	5
	α-Fe_2O_3 (hematite)	Fe^{3+}	0.37	−0.20	51.7	0.38	28
M2	FeS_2 (pyrite)	Fe^{3+}	0.32	0.61	—	0.39	21.5
	$Ca_2Fe^{2+}(PO_4)_2 \cdot 4H_2O$ (anapaite)	Fe^{2+}	1.18	2.51	—	0.39	17
	α-Fe_2O_3 (hematite)	Fe^{3+}	0.36	−0.20	51.3	0.39	26
	Fe_3O_4 (magnetite)	$Fe^{2.5+}$	0.66	—	46.2	0.40	14
		Fe^{3+}	0.28	—	49.4	0.39	7.5
	$Ca^2(Fe^{3+},Al)_3O(OH)(Si_2O_7)(SiO_4)$ (epidote)	Fe^{3+}	0.36	1.93	—	0.40	13
M3	FeS_2 (pyrite)	Fe^{2+}	0.32	0.60	—	0.39	23.8
	$Ca_2Fe^{2+}(PO_4)_2 \cdot 4H_2O$ (anapaite)	Fe^{2+}	1.19	2.51	—	0.39	20
	α-Fe_2O_3 (hematite)	Fe^{3+}	0.37	−0.20	51.4	0.40	23.7
	Fe_3O_4 (magnetite)	$Fe^{2.5+}$	0.64	—	46.5	0.40	11.9
		Fe^{3+}	0.28	—	49.7	0.39	7.2
	$Ca^2(Fe^{3+},Al)_3O(OH)(Si_2O_7)(SiO_4)$ (epidote)	Fe^{3+}	0.37	1.88	—	0.39	13.2
M4	$Mg_3Si_2O_5(OH)_4$ (antigorite)	Fe^{3+}	0.38	0.65	—	0.39	19
		Fe^{2+}	1.18	2.69	—	0.34	18
	α-Fe_2O_3 (hematite)	Fe^{3+}	0.37	−0.24	51.7	0.39	33
	Magnetite (Fe_3O_4)	$Fe^{2.5+}$	0.64	—	46.4	0.48	12.4
		Fe^{3+}	0.39	—	49.2	0.39	7.7
	$Ca^2(Fe^{3+},Al)_3O(OH)(Si_2O_7)(SiO_4)$ (epidote)	Fe^{3+}	0.36	2.10	—	0.39	9.5
I1	FeS_2 (pyrite)	Fe^{3+}	0.31	0.62	—	0.39	27
	$Ca_2Fe^{2+}(PO_4)_2 \cdot 4H_2O$ (anapaite)	Fe^{2+}	1.17	2.49	—	0.39	27.5
	Fe_3O_4 (magnetite)	$Fe^{2.5+}$	0.56	—	45.9	0.34	12.7
		Fe^{3+}	0.28	—	49.7	0.35	7.5
	α-Fe_2O_3 (hematite)	Fe^{3+}	0.41	−0.29	51.7	0.38	25.2
I2	FeS_2 (Pyrite)	Fe^{2+}	0.32	0.61	—	0.38	15.8
	$Ca_2Fe^{2+}(PO_4)_2 \cdot 4H_2O$ (anapaite)	Fe^{2+}	1.17	2.50	—	0.39	18.6
	α-Fe_2O_3 (hematite)	Fe^{3+}	0.32	−0.21	51.7	0.34	25
	Fe_3O_4 (magnetite)	$Fe^{2.5+}$	0.61	—	46.2	0.40	11.4
		Fe^{3+}	0.33	—	49.2	0.40	7.9
	$Fe^{3+}PO_4$ (heterosite)	Fe^{3+}	0.42	1.63	—	0.39	10.7
	$Ca_2Fe^{2+}(PO_4)_2 \cdot 4H_2O$ (anapaite)[a]	Fe^{2+}	1.20	2.10	—	0.39	10.6
I3	$CaFe^{2+}Si_2O_6$ (hedenbergite)	Fe^{2+}	1.19	2.29	—	0.38	15.8
		Fe^{3+}	0.34	0.68	—	0.39	17
	α-Fe_2O_3 (hematite)	Fe^{3+}	0.37	−0.21	51.4	0.33	24.5
	Fe_3O_4 (magnetite)	$Fe^{2.5+}$	0.66	—	46.2	0.40	12.7
		Fe^{3+}	0.28	—	49.3	0.39	7.1
	$Mg_3Si_2O_5(OH)_4$ (antigorite)	Fe^{3+}	0.38	0.85	—	0.39	8.8
		Fe^{2+}	1.14	2.78	—	0.38	16
I4	FeS_2 (pyrite)	Fe^{2+}	0.32	0.60	—	0.38	14.6
	$Ca_2Fe^{2+}(PO_4)_2 \cdot 4H_2O$ (anapaite)	Fe^{2+}	1.18	2.50	—	0.39	22.3
	α-Fe_2O_3 (hematite)	Fe^{3+}	0.39	−0.23	51.6	0.34	23.5
	Fe_3O_4 (magnetite)	$Fe^{2.5+}$	0.67	—	46.7	0.48	14.3
		Fe^{2+}	0.28	—	49.6	0.34	7.9
	$Fe^{3+}PO_4$ (heterosite)	Fe^{3+}	0.42	1.54	—	0.39	11.7
	$Ca_2Fe^{2+}(PO_4)_2 \cdot 4H_2O$ (anapaite)[a]	Fe^{2+}	1.19	2.10	—	0.39	5.5

Note: I.S., isomer shift; Q.S., quadrupole splitting; W, linewidth; B_{hf}, hyperfine magnetic field; and A, spectral area. The maximal experimental errors of hyperfine parameters (I.S. and Q.S.) and W are estimated to be ±0.03 $mm \cdot s^{-1}$, for B_{hf} is ±1.2 T (Tesla) and ±2% for the spectral area. [a] names "Anapaite with less defects" for presenting a decrease in the value of Q.S. in comparison with natural anapaite.

hyperfine splitting typical of bulk materials and no trace of superparamagnetic nature was observed since the calculated mean grain sizes are hundreds of micrometres, which suggests that it is possible to think that the presence of a doublet as a subspectrum does not belong to a superparamagnetic character. The fact that null magnetic hysteresis has not been detected (Table 6) supports the idea that the analyzed samples should not contain nanoparticles whose size is smaller than 10 nm. Although Mössbauer spectra measurements at 77 K were not taken, the absence of irreversibility features determined from temperature-dependent magnetic measurements, as discussed latter, confirms the absence of iron nanoparticles.

The main feature of all spectra is the magnetically split sextet due to the presence of two crystalline phases. Hematite (α–Fe_2O_3)

Table 6
Magnetic parameters derived from the $M(H)$ plots shown in Fig. 8. The ± (plus or minus) sing indicates the error in each figure.

Sample	Temp. (K)	M_S (emu/g)	M_R (emu/g)	M_R/M_S	H_s (Oe)	H_C (Oe)	Domain size (nm)
M1	5	0.710 ± 0.005	0.134 ± 0.004	0.189 ± 0.005	2,710 ± 25	302 ± 25	13
	300	0.699 ± 0.002	0.046 ± 0.003	0.066 ± 0.004	1,405 ± 24	91 ± 4	53
M2	5	1.109 ± 0.008	0.208 ± 0.005	0.188 ± 0.005	3,713 ± 25	252 ± 25	11
	300	1.137 ± 0.004	0.064 ± 0.005	0.056 ± 0.004	1,606 ± 25	31 ± 5	51
M3	5	0.318 ± 0.003	0.048 ± 0.002	0.151 ± 0.006	2,609 ± 25	191 ± 15	15
	300	0.276 ± 0.001	0.012 ± 0.004	0.043 ± 0.001	1,206 ± 25	71 ± 5	84
M4	5	0.420 ± 0.004	0.050 ± 0.002	0.119 ± 0.005	1,807 ± 25	121 ± 5	16
	300	0.276 ± 0.001	0.0249 ± 0.002	0.090 ± 0.007	1,305 ± 25	70 ± 5	64
I1	5	0.381 ± 0.003	0.058 ± 0.001	0.152 ± 0.002	2,910 ± 25	251 ± 25	15
	300	0.389 ± 0.002	0.023 ± 0.001	0.059 ± 0.003	1,004 ± 13	91 ± 8	51
I2	5	2.340 ± 0.01	0.369 ± 0.016	0.158 ± 0.007	2,810 ± 25	190 ± 15	89
	300	2.236 ± 0.008	0.133 ± 0.02	0.059 ± 0.008	3,211 ± 25	40 ± 5	38
I3	5	0.353 ± 0.003	0.054 ± 0.002	0.153 ± 0.006	1,406 ± 25	201 ± 15	15
	300	0.350 ± 0.001	0.024 ± 0.001	0.069 ± 0.002	1,405 ± 25	121 ± 4	58
I4	5	0.297 ± 0.003	0.068 ± 0.003	0.229 ± 0.01	3,211 ± 25	402 ± 15	18
	300	0.214 ± 0.008	0.024 ± 0.001	0.112 ± 0.006	3,011 ± 24	121 ± 5	75

with a magnetic hyperfine field of about 51 T, quadrupolar shift (Q.S.) from −0.19 to −0.23 mm·s^{-1} and an isomer shift (I.S.) of 0.37 mm·s^{-1} (Table 5). The negative values of the Q.S. agree with the weakly ferromagnetic (WF) phase, which is typical for bulk hematite (Lyubutin et al., 2009). Spinel magnetite (Fe_3O_4) in the $Fe^{2.5+}$ and Fe^{3+} sites with the hyperfine field (B_{hf}) accounting for 46 and 49 T, respectively, and the I.S. of 0.66 and 0.28 mm·s^{-1}, were also found. The difference of doublets d_{1-2}–d_{5-6}, in α-Fe_2O_3, is positive which means that Morin Temperature (T_M) is below room temperature that is in good agreement with De Grave & Vandenberghe but it cannot be concluded that its value is about 263 K due to the fact that this transition temperature does not solely depend on the particle size (De Grave & Vandenberghe, 1990; Nininger & Schroeer, 1978; Verbeeck et al., 1986) but also differs according to the interaction with other Fe components or with the other no-ferric magnetic components embedded in the crystallite. The magnetite relative absorption area ratio between the octahedral and tetrahedral sites for almost all the spectra, except for sample I4, is far away from the theoretical value of 1.8. This shift from the theorical value is probably due to the substitutions of Fe sites by other atoms present in the rest of mineral components detected by XRD. Moreover, the presence of impurity atoms in the hematite structure can contribute with the latter effect and they can lead to a distribution of local surroundings of iron atoms, which can explain the wider Mössbauer lines. In fact, coexisting with ferro- or ferrimagnetic components, the magnetic signal is easily screened by the other components as it is explained in more detail in the magnetometry analysis section.

Hematite and magnetite phases were not detected by XRD in all samples, except for samples M2 and M3. This fact might possibly be due to the exceptionally low Fe concentration (less than 4% as shown by EDX analysis) so that the limit of resolution of the diffractometer is affected and this phase is obscured by noise in the detector. The presence of two doublets was necessary to get a better fit in all spectra for each of the samples. One doublet has been assigned to the crystalline phase Anapaite ($Ca_2Fe^{2+}(PO_4)_2{\cdot}4H_2O$) that was found as a structural component in the six samples. The hyperfine parameters of this phase are listed in Table 5. It has a triclinic structure and there is only one type of octahedral site available for the Fe^{2+} cations in coordination with $O_2(OH_2)_4$. Anapaite has a strong paramagnetic behaviour which is maintained down to a temperature as low as 4.2 K. Studies about oxidation in solutions with various hydrogen peroxide (H_2O_2) concentrations (up to 20%) and Mössbauer spectra measurements at room temperature, to determine the percentage of new formation of Fe^{3+} cations due to oxidation, have revealed that the anapaite structure is unusually highly resistant against oxidation since eventually only a small amount of Fe^{2+} (~6.5%) is converted into Fe^{3+}. The Fe^{2+} doublet parameters are not modified by these small amounts of oxide. This feature of high resistance to being oxidized, does not allow a chemical transformation by simple changes in its surroundings at room temperature, which could explain why of this anapaite phase is present in six of the eight treated samples.

Antigorite ($Mg_3Si_2O_5(OH)_4$) has been detected in samples M4 and I3 whereas Hedenbergite ($CaFe^{2+}Si_2O_6$) phases have only been detected in the latter. A pair of doublets of proper hyperfine parameters of each phase indicate their presence (Table 5). Antigorite represents the group of serpentine minerals with polymorphs chrystolite and lizardite. Small amounts of iron in those serpentines yield hyperfine parameters of $I.S._{.Fe}$ = 1.14 mm·s^{-1} and Q.S. = 2.68–2.76 mm·s^{-1} for Fe^{2+}, and $I.S._{.Fe}$ = 0.37–0.42 mm·s^{-1} and Q.S. = 0.65–0.85 mm·s^{-1} for Fe^{3+} (O'Hanley & Dyar, 1993). Hedenbergite phase belongs to the group of pyroxenes and has a monoclinic structure where the Fe^{2+} cations are located in the N1 sites which are moderately distorted octahedra. Deviations from stoichiometry introduce a small amount of an Fe^{2+} doublet from N2 sites and a weak Fe^{3+} doublet.

Epidote mineral ($Ca_2(Fe^{3+},Al)_3O(OH)(Si_2O_7)(SiO_4)$) was found by a Zeeman doublet in the MS spectra corresponding to this phase in samples M2, M3, and M4. The epidote group is the class of silicate minerals named nesosilicates. Its structure is mainly monoclinic and consists of Al oxide and hydroxide chains linked by single-tetrahedra (SiO_4) and double-tetrahedra pyrosilicate (Si_2O_7). The Fe^{3+} is mainly located in a very irregular polyhedron called the M3 site and, hence, unusually large quadrupole splitting in the range of 1.9–2.1 mm·s^{-1} are observed for Fe^{3+}, whereas the isomer shifts 0.34–0.36 mm·s^{-1} clearly reflect the trivalent state (Fehr & Heuss-Aßbichler, 1997; Grodzicki et al., 2001).

Heterosite also is found forming part of the mineralogical composition of samples I2 and I3. This mineral, ideally $Fe^{3+}PO_4$, possesses the same structure as triphylite; however, with all M1 sites being vacant. Heterosite also forms a solid solution with purpurite, $MnPO_4$. The maximum-probability Q.S. values at RT were calculated to be 1.63 and 0.40 mm·s^{-1} due to the presence of two doublets where, based on the isomer shifts, both doublets are attributable to ferric cations. A value of 1.63 mm·s^{-1} for the quadrupole splitting is unusually high for Fe^{3+} species and is ascribed to a strong deformation of the M2 octahedra because of the presence of Mn^{3+} cations, which are Jahn–Teller active.

A Fe-bearing phase was found in samples I2 and I4 with I.S. and Q.S. values of 1.19 and 2.10 mm·s^{-1}, respectively (Table 5). In

Mössbauer's mineral handbook, at least similar hyperfine parameters of some ferric mineral were not found (Stevens et al., 1998). However, it is suggested that this phase could be related to the mineral anapaite and was named of "anapaite with less defects" due to a higher electronic symmetry of valence electrons around of the Mössbauer nuclei when compared with natural anapaite, obtaining in this way a considerable decrease in the Q.S. value (< 2.49 $m \cdot s^{-1}$) compared to natural anapaite.

In several samples, the pyrite phase was characterized by the existence of a doublet (Table 5). Pyrite is one of most abundant and widespread sulphides. This compound crystallizes in a cubic structure and contains divalent iron which is in a non-magnetic low spin state (FeII). Consequently, the Mössbauer spectra, consist of a doublet with low isomer shifts and moderate quadrupole splitting (Murad & Taylor, 1984). Overall, Mössbauer analysis showed the existence of common phases such as pyrite, anapaite, and hematite in samples M1, M2, M3, I1, and I4. All these similarities could be explained for the connection among them through the Moquegua river that may be acting as a carrier of these components between these two cities located in the Moquegua Region.

3.6. Magnetometry analysis

The magnetic properties of river sediment, sand, and soils currently are commonly used to study their formation, transportation, and deposition by wind or water; as well as to investigate temporal and geographical variations, climate change, pollution, and iron bio-mineralization around rivers and oceans (Evans & Heller, 2003; Stockhausen & Thouveny, 1999). The principle is based on the fact that most rocks, soils, and sands contain certain amounts of iron-bearing minerals, and thus, they respond in some way to an applied magnetic field. They are sensitive to a range of environmental processes, which makes magnetic measurements useful for detecting signals associated with environmental processes (Evans & Heller, 2003; Liu et al., 2012). However, interpretation often is often difficult and requires understanding of the underlying physics and chemistry.

Iron has been detected by the EDX technique in many of the sediment samples. Samples with the highest amount of iron were those collected after excavating 5 cm deep in the banks of the river (14.18% for sample M2 and 4.18% for sample I2). However, the only Fe-mineral found by XRD (hematite, see Table 2) was in sample M2 and none in sample I2. However, Mössbauer spectral analysis reveals the presence of other Fe-minerals which XRD does not detect due to their small quantities. In this section, a magnetometry technique is used to study the magnetic behaviour of the samples. Fe-minerals present different types of magnetic alignments such as ferromagnetism, antiferromagnetism, and ferrimagnetism. Whereas, silicates are typically paramagnetic, thus, the magnetic signal of the whole mineral can present a complex behaviour owing to the coexistence of different magnetic arrangements. The most common Fe-minerals, having magnetic signals are: goethite (α-FeOOH) (Dekkers, 1989; Franke et al., 2009; Lowrie & Heller, 1982), magnetite (Fe_3O_4) (Leon-Felix et al., 2017), hematite (α-Fe_2O_3) (Dekkers, 1988; Garming et al., 2007; Rochette et al., 1990; Salomé & Meynadier, 2004) titanomagnetite ($Fe_{2-x}Ti_xO_4$) (Garming et al., 2007; Salomé & Meynadier, 2004), pyrrhotite ($Fe_{1-x}S$ with $x = 0-0.2$) (Sagnotti et al., 2001; Snowball, 1991), and greigite.

Figure 7 shows the magnetization response of each sample as a function of temperature, obtained under an external field of 1 kOe. Note that samples M2 and I2 have the highest magnetization values as both contain the highest amount of Fe, as previously detected by EDX. Since both samples were collected 5 cm deep from the surface outside the river, these results suggest that iron contents are higher on the banks than on the bed of the river, and are kept safer buried than on the surface. The shape of the temperature dependence of the magnetization ($M(T)$) loops are typical for materials containing both paramagnetic and ferrimagnetic signals (Reis, 2013). The paramagnetic signal should come from the silicate components whereas the ferrimagnetism signal should come from magnetite (Fe_3O_4) (Franke et al., 2009) or titanomagnetite of the type $Fe_{2-x}Ti_xO_4$ with $x \leq 0.04$ (Garming et al., 2007; Salomé & Meynadier, 2004) (higher values, $x \geq 0.04$, are discarded since it has been reported that supresses the Verwey transition) (Kakol et al., 1994). In fact, all the samples have Verwey transition at 125 K which is a fingerprint of the presence of magnetite. The Verwey transition is caused by change in the amount of aligned spins due to change of crystalline structure in the magnetite from cubic to monoclinic (Jackson et al., 2011).

Around 35 K, the ZFC loops for most of the samples present the Besnus transition, revealing the presence of pyrrhotite (Gilder et al., 2011; Rochette et al., 1990, 2011). Pyrrhotite has a superstructure containing filled and vacant Fe(II) layers oriented to the $a-b$ plane (Morimoto et al., 1970). The ordered vacancies in pyrrhotite and the compensation of Fe(II) vacancies by Fe(III) produce a small net magnetization, which gives rise to ferrimagnetism up to its Néel temperature (598 K) (Morimoto et al., 1970). At the Besnus temperature (T_{Bes}), the direction of the magnetic easy axis changes from parallel to the c-axis to perpendicular to it (parallel to the basal $a-b$ plane) (Morimoto et al., 1970). This change in direction of

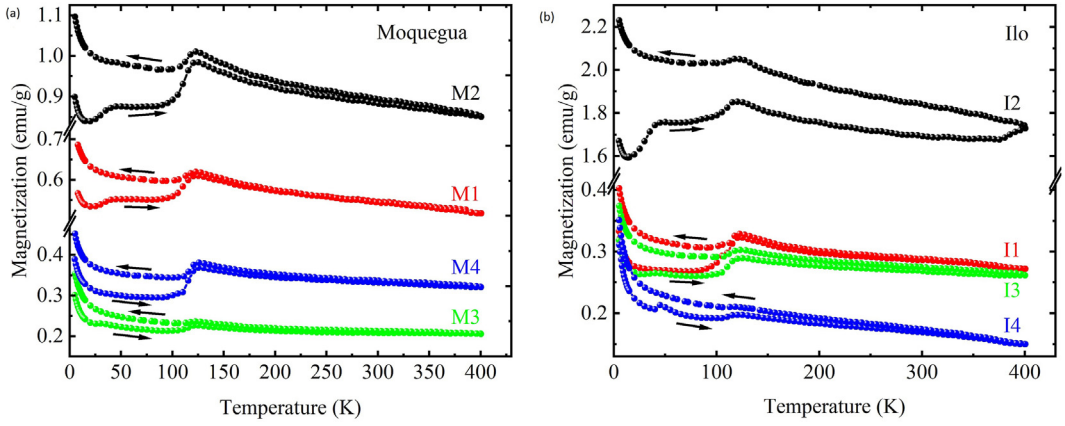

Fig. 7. Magnetization response as a function of the temperature for river sediment collected from (a) Moquegua and (b) Ilo cities, Peru. The measurements were taken under a magnetic field of 1 kOe. Note that samples collected 5 cm deep from the surface of the banks (samples M2 and I2) have the highest magnetization.

the magnetic easy axis might be related with crystallographic transition from triclinic below T_{Bes} to monoclinic above it (Morimoto et al., 1970).

Although pyrrhotite has not been previously detected by XRD, FTIR or Mössbauer spectroscopy, surely because its low amount, it is clearly identified here by the ferrimagnetic and ferromagnetic signals. The magnetometer equipment used in the current study is very sensitive to small magnetic moments, as produced by the magnetic components on the sediment samples in the current study. However, it is not clear if the pyrrhotite detected in the current study is natural or comes from mining activities operating in the Andes Mountains in the Moquegua region. However, the presence of pyrrhotite is harmful since it has been reported that it is thermodynamically unstable in the presence of oxygen and water. The weathering oxidation of pyrrhotite can release sulphur and generate hydrogen ions (H^+) which are dangerous for humans (Lindsay et al., 2015). Further studies are required to elucidate the origin of pyrrhotite along the Moquegua River.

Figure 8 shows the magnetic response of the river sediment as a function of the external magnetic fields taken at 5 and 300 K. The magnetic parameters estimated from the loops for all the samples are listed in Table 6 and plotted in the ESM S3. Similar to the $M(T)$ loops previously discussed, the highest magnetic saturation (M_S), magnetic remanence (M_R), and saturation field (H_S) values are estimated for samples M2 and I2, as expected, since they contain the highest amount of Fe. This is not the case for the coercivity (H_C) for which the highest values are estimated for samples M1 and I4, indicating that these materials are magnetically harder than the rest of the samples. The coercivity provides information on the concentration of magnetic domains in the samples. High coercivity indicates high concentrations of antiferromagnetic minerals (such as hematite and goethite), while low coercivity indicates higher presence of ferrimagnetic minerals (such as magnetite and pyrrhotite) (Salomé & Meynadier, 2004). Note that hematite has previously been detected by Mössbauer spectroscopy, but its Morin effect signal has not been detected in the previous $M(T)$ loops above because of its weak ferromagnetism signal. However, the relatively high coercivity of the hysteresis loops might confirm the hematite presence in most of the samples. Compared to samples M1 and I4, the low coercivity values estimated for samples M2 and I2 are related with the high amounts of magnetite and pyrrothite, confirming the previous $M(T)$ loops. It has also been suggested that anthropogenic pollution is mainly represented in minerals containing magnetite with soft magnetic hysteresis (Chaparro et al., 2004; Jordanova et al., 2004). If this assumption is correct, samples M2 and I2 might be the most anthropogenically polluted samples since they contain magnetite and have the lowest coercivity at room temperature among all the samples.

Jordanova et al. (2004) and Meena et al. (2011) also reports empirical correlations between the magnetic domain sizes and anthropogenic pollution in soils and sediment. According to Yang et al. (2007), coarse multi domain magnetite grains are very typical for anthropogenic pollution from industrial combustion processes or emission from cars. In contrast, fine-grained goethite is rather a typical product of soil weathering (Jambor & Dutrizac, 1998). Moreover, in typical sediment, hematite overgrows on oxidized magnetite and siliceous grains due to conversion of aged ferrihydrite (Franke et al., 2007; Walker et al., 1981). Furthermore, coarse pseudo-single domain (near multi-domain) magnetite have been reported to be typical from fluvial material (Desenfant et al., 2004; Franke et al., 2009). Eventually, coarse multidomain magnetite particles have been reported to be typical from polluted urban areas (Robertson et al., 2003). In the current case, according to Table 6, the magnetic domains sizes are smaller than 100 nm which is typical for sand and

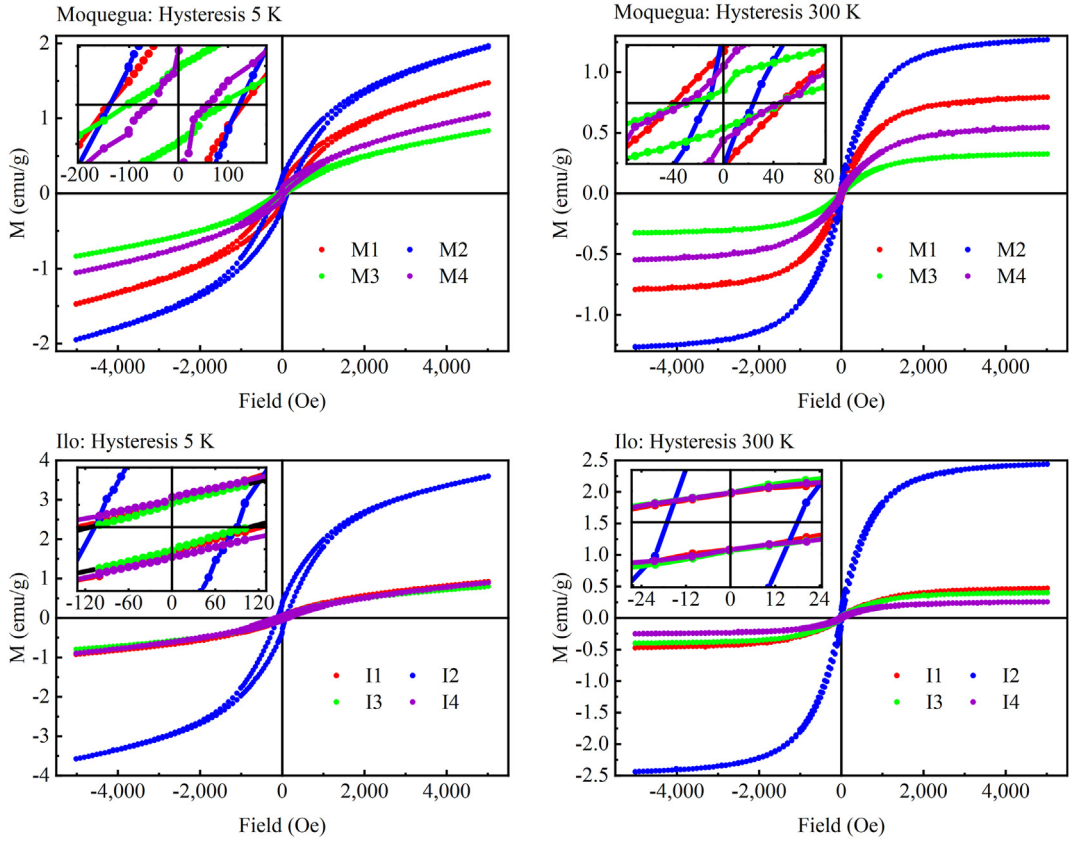

Fig. 8. Magnetic dependence as a function of applied fields for the river sediment collected from Moquegua and Ilo cities, Peru, and measured at 5 and 300 K.

soils (Jambor & Dutrizac, 1998). Further, among the samples, the biggest magnetic diameter (89 nm, calculated at 5 K) is that for sample I2. If the foregoing assumptions, together with the coercivity observations are correct, the samples collected at 5 cm down on the banks of the river might had been more exposed to anthropogenic pollution than the rest of the samples.

Linking the results in the current study with those previously reported (De Los Santos Valladares et al., 2022), it is confirmed that silicates are the main components of the sediment collected from the Moquegua River. Note that both studies, the elemental analysis by EDX detects the presence of Fe in most of the samples without identification of the corresponding Fe-minerals. In fact, in both studies, XRD is not able to identify the type of Fe-mineral perhaps because of their low amount in the sediment. However, in the current study, the iron components were correctly identified by Mössbauer spectroscopy and magnetometry. Specifically, Mössbauer spectroscopy reveals the presence of hematite and magnetite in nonstoichiometric state in almost all the samples, whereas magnetometry analysis identifies the presence of magnetite and pyrrhotite in some of the samples.

4. Conclusions

A series of physical and chemical techniques for the characterization of river sediment have been reviewed and tested to characterize sediment samples collected from two sites along the Moquegua River, Peru. Among the techniques, the microscopy analysis indicates that there is a variation in shape, size, and color of the granular samples, and those collected from the surface bank of the river have the smallest grains suggesting continuous crashing. The EDX and XRD techniques confirmed that the samples are composed mainly of Ca–, Na–, and K–Al silicates, which are typical for sand. FTIR confirms the XRD results and detects the presence of O–H and C–H stretching coming from organic matter present in the sediment. Thermogravimetry analysis confirmed the presence of organic and inorganic carbon which reacts with atmospheric air to show an apparent increase in mass in the TGA-DTA signals. Despite XRD only detecting Fe-minerals in samples M2 and M3 but not in I1–I4, M1, and M4, due to their low amount, Fe-minerals can be detected by their hyperfine parameters using Mössbauer spectroscopy and by their magnetic behaviour in magnetometry measurements. Mössbauer spectroscopy reveals the presence of hematite and magnetite in nonstoichiometric state in almost all the samples and some differences in Fe-mineral components on the samples coming from surface and excavated sites. Magnetometry analysis indicates that the samples consist of mostly paramagnetic, ferrimagnetic and antiferromagnetic domains belonging to the aluminium silicates and Fe-minerals, this technique identifies the presence of magnetite and pyrrhotite although they have not been detected by any other techniques.

Declaration of competing interest

The authors declare that they have no known competing financial interests or personal relationships that could have appeared to influence the work reported in this paper.

Acknowledgements

This research was supported by the Research Collaboration Agreement between the University of Cambridge, UK, and the National University of Moquegua, Peru (Agreement RG85120). The authors are thankful to J. Mendoza Quilli for his initial help in arranging the XRD plots. J.A.H. Coaquira thanks the Brazilian agencies National Council for Scientific and Technological Development (CNPq) and Fundacao de Apoio a Pesquisa do Distrito Federal (FAPDF) for financial support.

Electronic Supplementary Material

Supplementary data to this article can be found online at https://doi.org/10.1016/j.ijsrc.2024.03.003.

References

Ajasa, A. M. O., Bello, M. O., Ibrahim, A. O., Ogunwande, I. A., & Olawore, N. O. (2004). Heavy trace metals and macronutrients status in herbal plants of Nigeria. *Food Chemistry, 85*(1), 67–71.

Allard, T., Ponthieu, M., Weber, T., Filizola, N., Guyot, J.-L., & Benedetti, M. (2002). Nature and properties of suspended solids in the Amazon Basin. *Bulletin de la Societe Geologique de France, 173*(1), 67–75.

Alshibli, K. A., & Alsaleh, M. I. (2004). Characterizing surface roughness and shape of sands using digital microscopy. *Journal of Computing in Civil Engineering, 18*(1), 36–45.

Altuhafi, F., O'sullivan, C., & Cavarretta, I. (2013). Analysis of an image-based method to quantify the size and shape of sand particles. *Journal of Geotechnical and Geoenvironmental Engineering, 139*(8), 1290–1307.

Anbalagan, G., Prabakaran, A. R., & Gunasekaran, S. (2010). Spectroscopic characterization of indian standard sand. *Journal of Applied Spectroscopy, 77*(1), 124–128.

Bancroft, G. M., Maddock, A. G., & Burns, R. G. (1967). Applications of the Mössbauer effect to silicate mineralogy—I. Iron silicates of known crystal structure. *Cosmochimica Acta, 31*(11), 2219–2246.

Bancroft, G. M. (1973). *Mössbauer spectroscopy: An Introduction for inorganic chemists and geochemists*. London: McGraw-Hill.

Berger, K. G., & Akehurst, E. E. (1966). Some applications of differential thermal analysis to oils and fats. *International Journal of Food Science and Technology, 1*(3), 237–247.

Bowen, L. H., & Weed, S. B. (1984). Mössbauer spectroscopy of soils and sediments. In *Chemical Mössbauer spectroscopy* (pp. 217–242). New York: Plenum.

Carol, E. S., Kruse, E. E., & Tavani, E. L. (2012). Physicochemical characterization of sediments from the coastal wetland of Samborombón Bay, Argentina. *Journal of South American Earth Sciences, 34*, 26–32.

Chaparro, M. A. E., Bidegain, J. C., Sinito, A. M., Jurado, S. S., & Gogorza, C. S. G. (2004). Magnetic studies applied to different environments (soils and stream sediments) from a relatively polluted area in Buenos Aires Province, Argentina. *Environmental Geology, 45*(5), 654–664.

Corzo, M. A. C., Borja-Castro, L. E., Valladares, L. D. L. S., González, J. C., Medina, J. M., Quinde, A. T., … Rodriguez, V. A. P. (2022). Magnetic, structural and Mössbauer study of soils from an ancient mining area in Huancavelica-Peru. *Hyperfine Interactions, 243*(1), 3.

Das, N. (2007). *Modeling three-dimensional shape of sand grains using discrete element method*. Doctoral dissertation. Tampa, FL, U.S: Department of Civil and Environmental Engineering, University of South Florida.

De Grave, E., & Vandenberghe, R. E. (1990). Mössbauer effect study of the spin structure in natural hematites. *Physics and Chemistry of Minerals, 17*(4), 344–352.

De Los Santos Valladares, L., Bustamante Dominguez, A. G., Leon-Felix, L., Kargin, J. B., Mukhambetov, D. G., Kozlovskiy, A. L., Moreno, N. O., Flores Santibanez, J., Castellanos Cabrera, R., & Barnes, C. H. W. (2019). Characterization and Magnetic properties of hollow α-Fe_2O_3 microspheres obtained by sol gel and spray roasting methods. *Journal of Science: Advanced Materials and Devices, 4*, 483–491.

De Los Santos Valladares, L., Ccamapaza, J. L., Valencia Bedregal, R. A., Borja Castro, L. E., de Jesus Velazquez Garcia, J., Nimalika Perera, D. H., … Barnes, C. H. W. (2022). Physical and chemical characterization of sediments from an Andean river exposed to mining and agricultural activities: The Moquegua river, Peru. *International Journal of Sediment Research, 37*(6), 780–793.

de Vries, T. J., & Schrader, H. (1981). Variation of upwelling/oceanic conditions during the latest pleistocene through holocene off the central Peruvian coast: A diatom record. *Marine Micropaleontology, 6*(2), 157–167.

Dekkers, M. J. (1988). Magnetic properties of natural pyrrhotite Part I: Behaviour of initial susceptibility and saturation-magnetization-related rock-magnetic parameters in a grain-size dependent framework. *Physics of the Earth and Planetary Interiors, 3–4*(52), 376–393.

Dekkers, M. J. (1989). Magnetic properties of natural goethite-I. Grain-size dependence of some low- and high-field related rockmagnetic parameters measured at room temperature. *Geophysical Journal International, 2*(97), 323–340.

Desenfant, F., Petrovský, E., & Rochette, P. (2004). Magnetic signature of industrial pollution of stream sediments and correlation with heavy metals: Case study from South France. *Water, Air, and Soil Pollution, 152*(1), 297–312.

Dinnis, E. R. (1994). Book review "methods & applications D.L. Rowell, longman scientific & technical. Harlow: Longman group UK ltd.". *Journal of the Science of Food and Agriculture, 66*(4), 573–574.

Dodds, J. (2003). *Particle shape and stiffness- Effects on soil behavior*. M.S, tesis. Atlanta, GA, U.S: Department of Civil Engineering, Georgia Institute of Technology.

Dunn, J. G. (2000). *Thermogravimetry. Encyclopedia of analytical chemistry: Applications, theory and instrumentation*. New York: Wiley.

Dweck, J., Buchler, P. M., Coelho, A. C. V., & Cartledge, F. K. (2000). Hydration of a Portland cement blended with calcium carbonate. *Thermochimica Acta, 346*(1–2), 105–113.

Evans, M. E., & Heller, F. (2003). *Environmental magnetism: Principles and applications of enviromagnetics*. Amsterdam: Elsevier.

Fehr, K. T., & Heuss-Aßbichler, S. (1997). Intracrystalline equilibria and immiscibility along the join clinozoisite-epidote: An experimental and 57Fe Mössbauer study. *Journal of Mineralogy and Geochemistry, 172*(1), 43–67.

Franke, C., von Dobeneck, T., Drury, M. R., Meeldijk, J. D., & Dekkers, M. J. (2007). Magnetic petrology of equatorial Atlantic sediments: Electron microscopy results and their implications for environmental magnetic interpretation. *Palaeogeography, Palaeoclimatology, Palaeoecology, 22*(4), PA4207.

Franke, C., Kissel, C., Robin, E., Bonté, P., & Lagroix, F. (2009). Magnetic particle characterization in the Seine River system: Implications for the determination of natural versus anthropogenic input. *Geochemistry, Geophysics, Geosystems, 8*(10), GC002544.

Frondel, C. (1962). *Dana's system of mineralogy*. New York: Wiley.

Fu, H., & Quan, X. (2006). Complexes of fulvic acid on the surface of hematite, goethite, and akaganeite: FTIR observation. *Chemosphere, 63*(3), 403–410.

Gaál, F., Szöllózy, I., Arnold, M., & Paulik, F. (2007). Determination of the organic matter, metal carbonate and mobile water in soils simultaneous TG, DTG, DTA and EGA techniques. *Journal of Thermal Analysis and Calorimetry, 42*(5), 1007–1016.

Garming, J. F. L., von Dobeneck, T., Franke, C., & Bleil, U. (2007). Low-temperature partial magnetic self-reversal in marine sediments by magnetostatic interaction of titanomagnetite and titanohematite intergrowths. *Geophysical Journal International, 3*(170), 1067–1075.

Gilder, S. A., Egli, R., Hochleitner, R., Roud, S. C., Volk, M. W., Le Goff, M., & De Wit, M. (2011). Anatomy of a pressure-induced, ferromagnetic-to-paramagnetic transition in pyrrhotite: Implications for the formation pressure of diamonds. *Journal of Geophysical Research: Solid Earth, 116*(B10), B10101.

Greenwood, N. N., & Gibb, T. C. (1971). *Mössbauer spectroscopy*. London: Chapman & Hall.

Grodzicki, M., Heuss-Assbichler, S., & Amthauer, G. (2001). Mössbauer investigations and molecular orbital calculations on epidote. *Physics and Chemistry of Minerals, 28*, 675–691.

Gudbrandsson, S. (2013). *Experimental weathering rates of aluminium-silicates*. Doctoral dissertation. France: Department of Science de la Terre et des Planetes Solides. Université Paul Sabatier-Toulouse III.

Haghighizade, S. R., Sharahi, M. J., Mirhosseini, S. M., & Mousavi, M. (2017). Effect of gradation and particle shape on sand properties as coverage of beach soccer ground - details of a patent. *Annals of Applied Sport Science, 5*(3), 49–62.

Härdter, R., Rex, M., & Orlovius, K. (2005). Effects of different Mg fertilizer sources on the magnesium availability in soils. *Nutrient Cycling in Agroecosystems, 70*(3), 249–259.

Hatakeyama, T., & Liu, Z. (1998). *Handbook of thermal analysis*. New York: Wiley.

Hunter, M., Perera, D. H. N., Barnes, E. P. G., Lepage, H. V., Escobedo-Pacheco, E., Idros, N., … Barnes, C. H. W. (2024). Landscape-scale mining and water management in a hyper-arid catchment: The cuajone mine, Moquegua, southern Peru. *Water, 16*(5), 769.

Hutchins, D. A., Hare, C. E., Weaver, R. S., Zhang, Y., Firme, G. F., DiTullio, G. R., … Bruland, K. W. (2002). Phytoplankton iron limitation in the humboldt current and Peru upwelling. *Limnology & Oceanography, 47*(4), 997–1011.

Igisu, M., Nakashima, S., Ueno, Y., Awramik, S. M., & Maruyama, S. (2006). *In situ* infrared microspectroscopy of ~850 million-year-old prokaryotic fossils. *Applied Spectroscopy, 60*(10), 1111–1120.

Ilia, I., Stamatakis, M., & Perraki, T. (2009). Mineralogy and technical properties of clayey diatomites from north and central Greece. *Central European Journal of Geosciences, 1*(4), 393–403.

Ito, Y., & Nakashima, S. (2002). Water distribution in low-grade siliceous metamorphic rocks by micro-FTIR and its relation to grain size: A case from the kanto mountain region, Japan. *Chemical Geology, 189*(1–2), 1–18.

Jackson, M., Moskowitz, B., & Bowles, J. (2011). The magnetite Verwey transition. *The IRM Quartely, 20*, 1–11.

Jambor, J. L., & Dutrizac, J. E. (1998). Occurrence and constitution of natural and synthetic ferrihydrite, a widespread iron oxyhydroxide. *Chemical Reviews, 98*(7), 2549–2586.

Ji, J., Ge, Y., Balsam, W., Damuth, J. E., & Chen, J. (2009). Rapid identification of dolomite using a fourier transform infrared spectrophotometer (FTIR): A fast method for identifying heinrich events in iodp site U1308. *Marine Geology, 258*(1–4), 60–68.

Jordanova, D., Hoffmann, V., & Fehr, K. T. (2004). Mineral magnetic characterization of anthropogenic magnetic phases in the Danube River sediments (Bulgarian part). *Earth and Planetary Science Letters, 221*(1–4), 71–89.

Kakol, Z., Sabol, J., Stickler, J., Kozl, A., & Honig, J. M. (1994). Influence of titanium doping on the magnetocrystalline anisotropy of magnetite. *Physical Review B, 49*(18), 12767.

Khang, V. C., Korovkin, M. V., & Ananyeva, L. G. (2016). Identification of clay minerals in reservoir rocks by FTIR spectroscopy. *IOP Conference Series: Earth and Environmental Science, 43*(1), 012004.

Leon, L., Bustamante, A., Osorio, A., Olarte, G. S., De Los Santos Valladares, L., Barnes, C. H. W., & Majima, Y. (2011). Synthesis and characterization of hollow α-Fe_2O_3 sub-micron spheres prepared by sol-gel. *Hyperfine Interactions, 202*, 131–137.

Leon-Felix, L., Coaquira, J. A. H., Martinez, M. A. R., Goya, G. F., Sousa, M. H., De los Santos Valladares, L., Barnes, C. H. W., & Morais, P. C. (2017). Structural and magnetic properties of core-shell Au/Fe_3O_4 nanoparticles. *Scientific Reports, 7*, 41732.

Lindsay, M. B., Moncur, M. C., Bain, J. G., Jambor, J. L., Ptacek, C. J., & Blowes, D. W. (2015). Geochemical and mineralogical aspects of sulfide mine tailings. *Applied Geochemistry, 57*, 157–177.

Liu, T. Y., Chang, C. Y., & Chiou, T. J. (2009). The long-distance signaling of mineral macronutrients. *Current Opinion in Plant Biology, 12*(3), 312–319.

Liu, Q., Roberts, A. P., Larrasoaña, J. C., Banerjee, S. K., Guyodo, Y., Tauxe, L., & Oldfield, F. (2012). Environmental magnetism: Principles and applications. *Reviews of Geophysics, 4*(50), RG4002.

Lorenz, R. D., & Zimbelman, J. R. (2014). Sand. In *Dune worlds* (pp. 17–25). Berlin: Springer.

Lowrie, W., & Heller, F. (1982). Magnetic properties of marine limestones. *Reviews of Geophysics, 2*(20), 171–192.

Lyubutin, I. S., Lin, C. R., Korzhetskiy, Y. V., Dmitrieva, T. V., & Chiang, R. K. (2009). Mössbauer spectroscopy and magnetic properties of hematite/magnetite nanocomposites. *Journal of Applied Physics, 106*(3), 034311.

Mackenzie, F. T. (2004). *Sediments, diagenesis, and sedimentary rocks* (Vol. 7). Ámsterdam: Elsevier.

Madejová, J. (2003). FTIR techniques in clay mineral studies. *Vibrational Spectroscopy, 31*, 1–10.

Meena, N. K., Maiti, S., & Shrivastava, A. (2011). Discrimination between anthropogenic (pollution) and lithogenic magnetic fraction in urban soils (Delhi, India) using environmental magnetism. *Journal of Applied Geophysics, 73*(2), 121–129.

Meena, V. S., Maurya, B. R., Verma, J. P., & Meena, R. S. (2016). *Potassium solubilizing microorganisms for sustainable agriculture*. Berlin: Springer.

Meyer-Jacob, C., Vogel, H., Gebhardt, A. C., Wennrich, V., Melles, M., & Rosen, P. (2014). Biogeochemical variability during the past 3.6 million years recorded by FTIR spectroscopy in the sediment record of Lake El'gygytgyn, Far East Russian Arctic. *Climate of the Past, 10*(1), 209–220.

Minai, Y., & Tominaga, T. (1982). Mössbauer analysis of iron(II) and iron(III) in geological reference materials. *The International Journal of Applied Radiation and Isotopes, 33*(7), 513–515.

Morimoto, N., Nakazawa, H., Nishigucmi, K., & Tokonami, M. (1970). Pyrrhotites: Stoichiometric compounds with composition Fe n-1S n (n≥ 8). *Science, 168*(3934), 964–966.

Murad, E., & Taylor, R. M. (1984). The Mössbauer spectra of hydroxycarbonate green rusts. *Clay Minerals, 1*(19), 77–83.

Newkirk, A. E. (1960). Thermal methods of analysis. *Analytical Chemistry, 32*(12), 1558–1563.

Nininger, R. C., Jr., & Schroeer, D. (1978). Mössbauer studies of the Morin transition in bulk and microcrystalline α-Fe2O3. *Journal of Physics and Chemistry of Solids, 2*(39), 137–144.

O'Hanley, D. S., & Dyar, M. D. (1993). The composition of lizardite 1T and the formation of magnetite in serpentinites. *American Mineralogist, 3–4*(78), 391–404.

Ojima, J. (2003). Determining of crystalline silica in respirable dust samples by infrared spectrophotometry in the presence of interferences. *Journal of Occupational Health, 45*(2), 94–103.

Oudghiri, F., García-Morales, J. L., & Rodríguez-Barroso, M. R. (2014). Rapid screening of estuarine sediments properties using thermogravimetric analysis and attenuated total reflectance (ATR) by fourier transform infrared (FTIR) spectrometry. *Water, Air, and Soil Pollution, 225*(2), 1–10.

Oudghiri, F., García-Morales, J. L., & Rodríguez-Barroso, M. R. (2015a). Evaluation of sediments decontamination by chelating agents using thermogravimetric analysis. *International Journal of Environmental Research, 9*(2), 657–662.

Oudghiri, F., García-Morales, J. L., & Rodríguez-Barroso, M. R. (2015b). Novel use of TGA–FTIR technique to predict the pollution degree in marine sediments. *Infrared Physics & Technology, 72*, 52–57.

Parikh, S. J., Goyne, K. W., Margenot, A. J., Mukome, F. N. D., & Calderón, F. J. (2014). Soil chemical insights provided through vibrational spectroscopy. *Advances in Agronomy, 126*, 1–148.

Ramasamy, V., Murugesan, S., & Mullainathan, S. (2004). Characterization of minerals and relative distribution of quartz in Cauvery River dediments from Tamilnadu, India – a FTIR study. *Bulletin of Pure and Applied Science, 23F*(1–2), 1–7.

Ramasamy, V., Rajkumar, P., & Ponnusamy, V. (2009). Depth wise analysis of recently excavated Vellar River sediments through FTIR and XRD studies. *Indian Journal of Physics, 83*(9), 1295–1308.

Reig, F. B., Adelantado, J. V. G., & Moya Moreno, M. C. M. (2002). FTIR quantitative analysis of calcium carbonate (calcite) and silica (quartz) mixtures using the constant ratio method. Application to geological samples. *Talanta, 58*(4), 811–821.

Reis, M. (2013). *Fundamentals of magnetism*. Cambridge, MA, U.S.: Academic Press.

Robertson, D. J., Taylor, K. G., & Hoon, S. R. (2003). Geochemical and mineral magnetic characterisation of urban sediment particulates, Manchester, UK. *Applied Geochemistry, 18*(2), 269–282.

Rochette, P., Fillion, G., Mattéi, J. L., & Dekkers, M. J. (1990). Magnetic transition at 30–34 Kelvin in pyrrhotite: Insight into a widespread occurrence of this mineral in rocks. *Earth and Planetary Science Letters, 98*(3–4), 319–328.

Rochette, P., Fillion, G., & Dekkers, M. J. (2011). Interpretation of low-temperature data part 4: The low-temperature magnetic transition of monoclinic pyrrhotite. *The IRM Quartely, 21*(1), 1–7.

Rosén, P., Vogel, H., Cunningham, L., Reuss, N., Conley, D. J., & Persson, P. (2010). Fourier transform infrared spectroscopy, a new method for rapid determination of total organic and inorganic carbon and biogenic silica concentration in lake sediments. *Journal of Paleolimnology, 43*(2), 247–259.

Roy, B. N. (1987). Spectroscopic analysis of the structure of silicate glasses along the joint xMAlO2-(1−x)SiO2(M = Li, Na, K, Rb, Cs). *Journal of the American Ceramic Society, 70*(3), 183–192.

Sagnotti, L., Macrì, P., Camerlenghi, A., & Rebesco, M. (2001). Environmental magnetism of late Pleistocene sediments from the Pacific margin of the Antarctic Peninsula and interhemispheric correlation of climatic events. *Earth and Planetary Science Letters, 192*, 65–80.

Salomé, A. L., & Meynadier, L. (2004). Magnetic properties of rivers sands and rocks from Martinique Island: Tracers of weathering? *Physics and Chemistry of the Earth, 13–14*(29), 933–945.

Schnitzer, M., Turner, R. C., & Hoffman, I. (1964). A thermogravimetric study of organic matter of representative Canadian podzol soils. *Canadian Journal of Soil Science, 1*(44), 7–13.

Senthil Kumar, R., & Rajkumar, P. (2013). Characterization of minerals in air dust particles in the state of Tamilnadu, India through ftir spectroscopy. *Atmospheric Chemistry and Physics Discussions, 13*(8), 22221–22248.

Smart, P., & Tovey, N. K. (1981). *Electron microscopy of soil and sediments: Examples*. New York: The Claredon Press, Oxford University Press.

Snowball, I. F. (1991). Magnetic hysteresis properties of greigite (Fe3S4) and a new occurrence in Holocene sediments from Swedish Lappland. *Physics of the Earth and Planetary Interiors, 1–2*(68), 32–40.

Stanienda, K. J. (2016). Carbonate phases rich in magnesium in the Triassic limestones of the eastern part of the Germanic Basin. *Carbonates and Evaporites, 31*(4), 387–405.

Stevens, J. G., Khasanov, A. M., Pollak, H., & Zhe, L. (1998). *Mössbauer mineral handbook*. Mössbauer Effect Data Center Asheville.

Stockhausen, H., & Thouveny, N. (1999). Rock-magnetic properties of eemian maar lake sediments from massif central, France: A climatic signature? *Earth and Planetary Science Letters, 3*(173), 299–313.

Tao, Q., Su, L., Frost, R. L., Zhang, D., Chen, M., Shen, W., & He, H. (2014). Silylation of mechanically ground kaolinite. *Clay Minerals, 49*(4), 559–568.

Temuujin, J., Burmaa, G., Amgalan, J., Okada, K., Jadambaa, T., & Mackenzie, K. J. D. (2001). Preparation of porous silica from mechanically activated kaolinite. *Journal of Porous Materials, 8*(3), 233–238.

Thamaphat, K., Limsuwan, P., & Ngotawornchai, B. (2008). Phase characterization of TiO2 powder by XRD and TEM. *Agriculture and Natural Resources, 42*(5), 357–361.

Theodosoglou, E., Koroneos, A., Soldatos, T., Zorba, T., & Paraskevopoulos, K. M. (2010). Comparative Fourier transform infrared and X-ray K-feldspars, 2010 Proceedings of the 12th International Congress *Bulletin of the Geological Society of Greece*, 2752–2761.

Tironi, A., Trezza, M. A., Irassar, E. F., & Scian, A. N. (2012). Thermal treatment of kaolin: Effect on the pozzolanic activity. *Procedia Materials Science, 1*, 343–350.

Tominaga, T., & Minai, Y. (1984). *Applications of Mössbauer spectroscopy to environmental and geochemical studies*. Boca Raton, FL, U.S.: CRC Press.

Tuttle, O. F., & Bowen, N. L. (1950). High-temperature albite and contiguous feldspars. *The Journal of Geology, 58*(5), 572–583.

Uebel, E., & Heinsdorf, D. (1997). Results of long-term K and Mg fertilizer experiments in afforestation. *Forest Ecology and Management, 91*(1), 47–52.

Vaculíková, L., & Plevová, E. (2005). Identification of clay minerals and micas in sedimentary rocks. *Acta Geodynamica et Geomaterialia, 2*(2), 167–175.

van Cappellen, P., & Wang, Y. (1996). Cycling of iron and manganese in surface sediments: A general theory for the coupled transport and reaction of carbon, oxygen, nitrogen, sulfur, iron, and manganese. *American Journal of Science, 296*(3), 197–243.

Verbeeck, A. E., De Grave, E., & Vandenberghe, R. E. (1986). The effect of the particle morphology on the Mössbauer effect in α-Fe_2O_3. *Hyperfine Interactions, 1*(28), 639–642.

Vogel, H., Rosén, P., Wagner, B., Melles, M., & Persson, P. (2008). Fourier transform infrared spectroscopy, a new cost-effective tool for quantitative analysis of biogeochemical properties in long sediment records. *Journal of Paleolimnology, 40*(2), 689–702.

Walker, T. R., Larson, E. E., & Hoblitt, R. P. (1981). Nature and origin of hematite in the moenkopi formation (triassic), Colorado plateau: A contribution to the origin of magnetism in red beds. *Journal of Geophysical Research: Solid Earth, 86*(B1), 317–333.

Wang, Y., & van Cappellen, P. (1996). A multicomponent reactive transport model of early diagenesis: Application to redox cycling in coastal marine sediments. *Geochimica et Cosmochimica Acta, 60*(16), 2993–3014.

Webb, D. A. (1939). The sodium and potassium content of sea water. *Journal of Exprimental Biology, 16*(2), 178–183.

Yang, T., Liu, Q., Chan, L., & Liu, Z. (2007). Magnetic signature of heavy metals pollution of sediments: Case study from the East Lake in Wuhan, China. *Environmental Geology, 52*(8), 1639–1650.

Yoo, J., Shim, T., Hur, J., & Jung, J. (2016). Role of polarity fractions of effluent organic matter in binding and toxicity of silver and copper. *Journal of Hazardous Materials, 317*, 344–351.

Zhang, M., Wruck, B., Barber, A. G., Salje, E. K. H., Carpenter, M. A., Street, D., & Cb, C. (1996). Phonon spectra of alkali feldspars: Phase transitions and solid solutions. *American Mineralogist, 81*, 92–104.